Title: Stored potential energy and elastic properties alterations after restoring dentin with Zn-containing amalgam materials.

Short title: Nano-DMA and Raman analysis of dentin restored with Zn-containing materials.

Authors: Manuel Toledano[a], Estrella Osorio[a], Fátima S. Aguilera[a], Manuel Toledano-Osorio[a], Modesto T.López-López[b], Raquel Osorio[a].

Institution: [a]University of Granada, Faculty of Dentistry, Dental Materials Section.

Address: [a]University of Granada, Faculty of Dentistry, Dental Materials Section

Colegio Máximo de Cartuja s/n

18071 – Granada - Spain.

[b]University of Granada, Faculty of Science, Applied Physics Department

Fuente Nueva s/n

18071 – Granada - Spain.

*Corresponding author: Prof. Manuel Toledano

University of Granada, Faculty of Dentistry

Dental Materials Section

Colegio Máximo de Cartuja s/n

18071 – Granada - Spain.

Tel.: +34-958243788

Fax: +34-958240809

Email: toledano@ugr.es

Abstract

The aim of this research was to assess and quantify the mechanical and chemical behavior of sound and caries-affected dentin (CAD), after the placement of Zn-free *vs* containing amalgam restorations, and thermocycling. Peritubular and intertubular dentin were evaluated using, a) nanoindenter in scanning mode; the load and displacement responses were used to perform the nano-Dynamic mechanical analysis and to estimate the complex (E^*) and storage modulus (E'); b) Raman spectroscopy, to describe the principal component analysis (PCA) and the hierarchical cluster analysis (HCA). Assessments were performed before restoration placement, after restoration removal, and after 3 months of storage with thermocycling (100,000cy/5 ºC and 55 ºC). When CAD was treated with Zn-containing restorations, thermocycling augmented the differences between E^* and E', at both peritubular and intertubular dentin. The complex and storage modulus were minimum at intratubular dentin of CAD restored with Zn-containing restorations. The relative presence of minerals, crystallinity referred to phosphate and crosslinking of collagen increased at both peritubular and intertubular dentin of CAD restored with Zn-containing restorations. Nature and secondary structure of collagen augmented, in general, in those groups, except at ratio amide III/CH_2 and AGEs-pentosidine. Hierarchical cluster analysis revealed different levels of dentin maturation, after thermocycling.

1. Introduction

Dentin occupies the majority of each tooth by weight (70 % the inorganic hydroxyapatite crystal, 18% the organic matter) and volume (50% hydroxyapatite crystal, 25% the organic tissue), exhibiting a complex hierarchical structure (Ryou et al., 2015). The most original characteristic of its microstructure is the network of dentinal tubules, hollow cylinders, comprised between the pulp and the dentin-enamel junction; they are parallel, micrometer-sized, collagen-poor, containing a peritubular cuff of hypermineralized (apatite crystals), dentin (approx. 0.5-1 µm in thickness) (Xu and Wang, 2012). Intertubular dentin occupies the zone among the tubules, and is made of organic matrix (collagen fibers) and nanoscopic crystals of apatite similar to that of peritubular dentin (Wang et al., 2007). Those structural differences make consider dentin as a biological composite (Ryou et al., 2015). Sound dentin or non carious dentin is not the substrate most frequently involved in clinical dentistry. Instead, dentists usually must clinically handle irregular dentin substrates such as carious dentin (Wang et al., 2007). Carious dentin consists of a superficial opaque zone of caries-infected dentin and a deeper or transparent zone of caries-affected dentin (CAD) (Fusayama, 1979), located adjacent to the intact dentin. This inner zone (CAD) is partially, but highly heterogeneously, demineralized. Usually, caries-affected dentin is remineralizable due to sound collagen fibers, fuchsin-unstainable, surrounded by hydroxyapatite crystals, free of bacteria and should ideally be preserved during tooth preparation (Vaseenon, 2011). Three zones can be observed in a caries-affected dentin lesion (Fusayama, 1993), *i)* the turbid zone, where the peritubular dentin is not present because of the demineralization process, though the intertubular dentin is identifiable but demineralized (Marshall et al., 1997), and tubules are free of mineral occlusion; *ii)*

in the transparent zone, both peritubular and intertubular are present, but typical character as a rhomboid-shaped β-tricalcium phosphate mineral crystals, termed whitlockite (Frank et al., 1964), are occupying the lumen of tubules; *iii)* in the sub-transparent zone, tubules are usually and partially occluded with mineral, but the amount of mineral in intertubular dentin might not be normal (Marshall et al., 1997). Since these alterations are of great clinical significance and their influence on the remineralization process requires clarification, recent advances of some dental materials (Toledano et al., 2015a) might contribute to explain this mineral precipitation.

Dental amalgam and resin composite are used by dentists to restore teeth diseased by dental caries. Failure of restorations is mainly due to secondary caries in resin composites and to tooth fracture in amalgam restorations (Donmez et al., 2005; Opdam et al., 2010; Spencer et al., 2014). Dental amalgam was introduced in clinical dentistry over 150 years ago. It represents a dental restorative filling material alloy that consists of approximately 50% mercury with the balance including silver, tin, copper, and other trace metals. Dental amalgam has provided a valuable and relatively inexpensive service for patients ever since. Improved clinical performance of amalgam restorations, as measured by a reduction in marginal fracture, may be related to the presence of zinc in the amalgam alloy (Anusavice, 2003). Zn-containing amalgams are alloys with more than 0.01 wt% zinc; those containing less than 0.01 wt% of zinc are known as Zn-free amalgams (Anusavice, 2003). Zn-containing amalgams enhanced the physical, mechanical, electro-chemical properties of the restoration, and the fatigue resistance of the amalgam microstructure (Watkins et al., 1995). Zn-rich products at the tooth-amalgam interface, as $ZnSn(OH)^6$, ZnO_2, and Zn^{++} free (Scholtanus et al., 2013), improved the sealing of the dentin-amalgam interface, enhancing the clinical lifetime of this restoration (Marshall et al., 1997). In addition, the use of zinc-containing materials

may reduce the collagen degradation mediated by matrix metalloproteinases (MMPs) within the carious dentin by protecting sensitive cleavage sites of collagen within the demineralized dentin (Osorio et al., 2011). Zinc may not only act as an inhibitor of MMPs, but may also influence signaling pathways and stimulate a metabolic effect in hard tissue mineralization (Hoppe et al., 2011). It may also be that effective inhibitors of MMPs placed at the interface may protect the seed crystallite-sparse collagen from degradation, allowing them to become remineralized (Liu et al., 2011). Reincorporation of mineral into the demineralized dentin matrix is important since the mineral precipitated may work as a constant site for further nucleation, and the remineralized subsurface of the tissue may be more resistant to subsequent acid attack. Zinc has also been shown to inhibit dentin demineralization (Takatsuka et al., 2005). These effects make zinc attractive for use as therapeutic agent in the fields of hard and soft tissue engineering. Thereby, the contemporary idea of minimally invasive operative treatment, where therapeutic restorations are performed to combat the carious process and remineralize the dental hard tissues, may be satisfied by using such Zn-containing amalgam systems. Previous outcomes have demonstrated that Zn-containing amalgams promoted an increase of nanomechanical properties, and a general augmentation of mineral gradients, ratios and crystallinity in partially mineral-depleted dentin surfaces, after submitting the restorations to an *in vitro* load cycling protocol (Toledano et al., 2015a, 2015b). Therefore, specific Zn-containing amalgams do have therapeutic and protective effects for inducing mineral precipitations within the partially demineralized caries affected dentin-amalgam interface. Nevertheless, the clinical significance of these results might be jeopardized as they were not performed with thermo-cycling challenge, which may compromise the nanostructure of dentin.

Temperature is a main decisive factor for the survival of collagen (Collins et al., 2002). In addition to the rich content and structural stability, sufficient thermal stability of amino acids is essential for the survival of type I collagen peptides (Wang et al., 2012). The effect of heat has been investigated in various collagenous non-spinal tissues (Bass et al., 2004), but seldom in dentin collagen. Dental architecture is quite different from these other tissues and it is not clear that prior results can be directly extrapolated. Thermal cycling is conventionally used to simulate the thermal changes that occur in the oral cavity during eating, drinking, or breathing which may stress the interface between restoratives and dentin. Mechanical stresses induced by differential thermal changes can directly induce stress concentration, fatigue propagation, crack, fracture, and fluid flow through this restorative interface (Mazzitelli et al., 2012). On the other hand, the mechanism of thermal and mechanical stability improvement, with respect to enzymatic degradation, is also thought to result from a decrease in the configurational entropy of the collagen through enhanced intra- or intermolecular bonding (Miles et al., 1999).

It is of interest to examine, with nano-dynamic mechanical analysis (nano-DMA), the complex modulus of the superficial dentin below the amalgam restorations submitted to thermo-cycling. This value should not be confused with Young's modulus which represents the tensile elastic modulus measured in a linear elastic material producing plastic deformation. On the other hand, the complex modulus can be decomposed into storage (elastic) and loss (damping) modulus components (Wilkinson et al., 2015). Even more, it has been stated that the nano-DMA analysis shows that the dampening (or viscous) behavior of the tissue is much more sensitive to the structural changes that occur with the oral function than the quasi-static behavior (Ryou et al., 2015). Thereby, it is required the capacity to absorb thermal shock waves and alleviate stresses, at this locations, in order to prevent crack propagation across the boundary

between the two phases of dentin and thus, may serve as useful biomimetic models for joining mechanically dissimilar biomaterials to restore form and function (Marshall et al., 2001). In this investigation, nano-DMA was used to evaluate mechanical behavior of human dentin, *i.e.*, the complex, storage and loss moduli for the underlying intertubular and peritubular dentin, using equations. This study was complemented with Raman spectroscopy and cluster analysis, that offer nondestructive measures and provide an insight on biochemical nature, molecular structure and scattering techniques, as spectroscopies of tissue. It is used as a quantitative chemical assessment methodology for biological samples in conjunction with the fact that the Raman peak intensity is proportional to the number of molecules within the volume of the scanned area (Milly et al., 2014). It is a sensitive method capable of identifying individual spectral bands arising from the inorganic calcium phosphate crystals and the protein/lipid constituents of dentin (Wang et al., 2009). Micro-Raman mapping technique appeares to offer a powerful method to directly analyze the dentin interface and the mineral content and distribution after placing the amalgam and the application of thermal stimuli. Various methods of multivariate analysis (Toledano et al., 2014a, Almahdy et al., 2012), like principal component analysis (PCA), hierarchical cluster analysis (HCA) and clustering k-means (KMC) have been established for analyzing two dimensional *data*. This is the first nano-DMA and Raman-based characterization of dentin below amalgam restorations.

In the present investigation, nano-DMA and Raman analysis were used to evaluate the mechanical and chemical behavior of sound and caries-affected dentin, and quantify the changes that take place after Zn-free *vs* containing restorations. The complex and storage modulus, and both mineral and organics chemical changes were evaluated for the intertubular and peritubular dentin. The tested null hypothesis was

that there are no differences in the mechanical properties and chemistry of inter- and peritubular dentin of sound and caries-affected substrata after removal of Zn-free *vs* containing restorations submitted to thermo-cycling.

2. Materials and Methods

2.1. Specimen preparation and thermocycling

Twelve extracted carious third molars without opposing occlusion were employed for the study. They were stored in 0.01% (w/v) thymol at 4º C for less than 1 month. Teeth were collected after written patients' informed consent (20 to 40 yr of age), under a protocol approved by the Institution Review Board. Specimens were randomly assigned to three groups (n= 4) according to: 1) untreated dentin, 2) Zn-free amalgam and, 3) Zn-containing amalgam. The inclusion criteria for carious dentin substrate were that the caries lesion, surrounded by sound dentin, was limited to the occlusal surface and it extended at least half the distance from the enamel-dentin junction to the pulp chamber. To obtain caries affected dentin, grinding was performed by using the combined criteria of visual examination, surface hardness using a dental explorer, and staining by a caries detector solution (CDS, Kuraray Co., Ltd., Osaka, Japan). Using this procedure it was removed all soft, stainable, carious dentin. It was left the relatively hard, caries-affected non staining dentin, on the experimental side. Flat mid-coronal sound dentin, and caries affected dentin surfaces surrounded by sound dentin, were exposed using a hard tissue microtome (Accutom-50; Struers, Copenhagem, Denmark) equipped with a slow-speed, water-cooled diamond wafering saw (330-CA RS-70300, Struers, Copenhagen, Denmark).

Dentin discs (2.5 mm thick) were sectioned (Isomet 4000, Buehler, Lake Bluff, IL, USA) from the mid-coronal portion of each tooth, and were polished through SiC

abrasive papers up to 4,000-grit with a final polishing procedure performed with diamond pastes (Buehler-MetaDi, Buehler Ltd. through 1 μm down to 0.25 μm. The specimens were treated in ultrasonic bath (Model QS3, Ultrawave Ltd, Cardiff, UK) containing deionized water [pH 7.4] for 5 min at each polishing step.

Two third of teeth were restored with amalgam. Two self threading titanium retentive pins (4.4 mm length) (STP Restorative Dentsply Maillefer, Ballaigues, Switzerland) were used to retain the amalgam restorations, by using copper bands (Copper Bands, Hard. AB Dentatus, Spånga, Sweden), surrounding the prepared dentin discs. A tile of Zn-free *vs* Zn-containing dental amalgam was condensed on top of the disc surfaces in a layer of at least 3 mm thick. Finally, the amalgam surfaces were finished with hand instruments. The detailed composition of each amalgam is shown in Table 1. The other third remained untreated as control.

Table 1. Composition of amalgams used in the present study.

RESTORATIVES	COMPOSITION	
	Alloy powder	**Weight %**
Megalloy EZ®* (Zn-free)	Silver	56.7 %
	Tin	28.6 %
	Copper	14.7%
The recommended alloy to mercury ratio by mass is approximately 1.3:1.		
Dispersalloy®* (Zn-containing)	Silver	69 %
	Tin	18 %
	Copper	12 %
	Zinc	1 %
The recommended alloy to mercury ratio by mass is approximately 1:1.		

* Dentsply DeTrey GmbH Konstanz, Germany.

Restored teeth were stored for 24 hours in simulated body fluid solution (SBFS), pH 7.45, at 37 ºC, and then submitted to the test of thermal cycling (100,000cy/5 ºC and 55 ºC, during 3 months) (SD Mechatronik GmbH, Germany), in PBS (phosphate buffered saline) (Ref. D8662, Sigma-Aldrich, St Louis, USA). The amalgam tiles were removed from the discs by cutting away the amalgam around the retentive pins. The cut blocks of amalgams were eliminated with a lab tweezers from the dental working surface. Then, in order to eliminate the debris from the dentin surface the specimens were treated in an ultrasonic bath (Model QS3, Ultrawave Ltd, Cardiff, UK) containing deionized water [pH 7.4] for 5 min before the further analysis. All specimens were submitted to nano-DMA, imaging analysis, Raman spectroscopy and clusters analysis.

2.2. Nano-DMA and Atomic Force Microscope imaging analysis

Property mappings were conducted using a HysitronTi 950 nanoindenter (Hysitron, Inc., Minneapolis, MN) equipped with nano-DMA III, a commercial nano-DMA package. The nanoindenter tip was calibrated against a fused quartz sample using a quasistatic force setpoint of 2µN to maintain contact between the tip and the sample surface. A dynamic (oscillatory) force of 2 µN was superimposed on the quasistatic signal at a frequency of 200 Hz. Based on a calibration-reduced modulus value of 69.6 GPa for the fused quartz, the best-fit spherical radius approximation for tip was found to be 85 nm, for the selected nano-DMA scanning parameters. Modulus mapping of our samples was conducted by imposing a quasistatic force setpoint, $F_q=2$ µN, to which we superimposed a sinusoidal force of amplitude $F_A=0.10$ µN and frequency f=100 Hz. The resulting displacement (deformation) at the site of indentation was monitored as a function of time. Data from regions approximately 25x25 µm in size were collected using a scanning frequency of 0.2 Hz. Each scan resulted in a 256 x 256 pixel data

array. Specimens were scanned in the hydrated condition by the application of a layer of ethylene glycol over the specimen surface to prevent water evaporation during the analysis.

Under steady conditions (application of a quasistatic force) the indentation modulus of the tested sample (E) was obtained by application of different models that relate the indentation force (F) and depth (D). Most of these theories assume proportionality between the force and the indentation modulus (Hertz, 1881; Oliver and Pharr, 1992; Han et al., 2011). Statistical analyses were performed with ANOVA and Student Newman Keuls multiple comparisons tests. $P<0.05$ was set for significance.

During the indentation mode, single indents were introduced on either the intertubular dentin or intratubular dentin (in the group of Zn-containing amalgams), and the peritubular cuff. In this mode of evaluation the tip geometry and corresponding contact area was determined using the conventional approach with a fused silica standard sample (Oliver and Pharr, 1992). For intertubular dentin, discrete indentations were made in locations that were at least 3 μm from a peritubular cuff or previous indents. For the peritubular cuffs, only single indentations were performed on a cuff due to the limited cuff thickness.

An atomic force microscope (AFM Nanoscope V, Digital Instruments, Veeco Metrology group, Santa Barbara, CA, USA) equipped with a triboscope indentor system (Hysitron Inc., Minneapolis, MN) was employed in this study for topography mappings. The imaging process was undertaken inside a wet cell in a fully hydrated state, using the tapping mode, with a calibrated vertical-engaged piezo-scanner (Digital Instrument, Santa Barbara, CA, USA). A 10-nm-radius silicon nitride tip (Veeco) was attached to the end of an oscillating cantilever that came into intermittent contact with the surface at the lowest point of the oscillation. Changes in vertical position of the AFM tip at

resonance frequencies near 330 kHz provided the height of the images registered as bright and dark regions. 15 x 15 μm digital images were recorded from each dentin interface, with a slow scan rate (0.1 Hz). To facilitate dentin surfaces observation, AFM images have been tilted using a specific software (NanoScope Analysis v. 1.40, Bruker Corporation, Billerica, MA, USA).

2.3. Raman spectroscopy and clusters analysis

A dispersive Raman spectrometer/microscope (Horiba Scientific Xplora, Villeneuve d´Ascq, France) was used to analyze dentin surfaces. A 785-nm diode laser (100 mW sample power) and an X100/0.90 NA air objective were employed. Raman signal was acquired using a 600-lines/mm grating centered between 200 and 1,700 cm^{-1}.Chemical mapping of the surfaces was performed and submitted to K-means cluster (KMC) analysis using the multivariate analysis tool (ISys® Horiba), which includes statistical pattern to derive the independent clusters. The output from a clustering algorithm was basically a statistical description of the cluster centroids with the number of components in each cluster. Multivariate Raman images were produced, which overlapped different univariate images, derived from the integration of a specific Raman band after subtraction of the local baseline. A suitable selected Raman band represents a known chemical compound, and its spatial distribution is represented by a single color. The intensity of the color is determined by the integrated intensity of the selected Raman band. The K-means clustering is a method of cluster analysis based on a centroid model which aims to partition n observations into k clusters in which each observation belongs to the cluster with the nearest mean (Almahdy et al., 2012). The biochemical content of each cluster was analyzed using the average cluster spectra. Principal component analysis (PCA) decomposed data set into a bilinear model of linear independent

variables, the so-called principal components (PCs). It was hence used for identifying significant spectral differences among distinct substrata. For hierarchical cluster analysis (HCA) Raman imaging, each dataset was assessed to automatically distinguish regions of the scanned area with different Raman features (Vanna et al., 2015). For each specimen, a 1μm x 1μm area of the surface was mapped using 0.2 μm spacing at X and Y axes, at 100x magnification. A total of 25 points were performed per map. In the cluster analysis routine, PCA scores were taken as input variables, squared Euclidean distances were used as distances measures, and Ward's algorithm was used to partition Raman spectra into cluster. Clusters were created following Ward's technique (HCA) and the dendrogram was calculated applying three factor spectra or principal components, corresponding to three different histological locations of both sound and caries affected dentin surfaces. The employed HCA is an agglomerative clustering methods, which starts with each spectrum defining it´s, own cluster. Then, each cycle of the method involves the calculation of all possible inter-cluster distances based on the Ward's method, followed by the joining of two clusters based on the minimization of within-cluster variance. Three levels of HCA clustering were used in order to obtain HCA Raman images with a good description of the dentin composition. Each cluster was assigned to a different color, thus obtaining a false color-image of the substrate on the basis of similar spectral features. For each point of analysis, all spectra described for each cluster were averaged to obtain the mean cluster spectrum. Each mean cluster spectrum was then corrected by subtracting the mean spectrum of the background measured around the specific location of analysis. The aim of a factor analysis lies in the effective reduction of the dataset dimension while maintaining a maximum of information. This method was used to model the data and to determine spectral variances associated for data differentiation. It resulted in the calculation of a new

coordinate system whereby variations of the dataset is described via new axes, principal components (PCs). As the cluster centroids are essentially means of the cluster score for the elements of cluster, the mineral and organic components of substrata were examined for each cluster.At this point, the relative presence of mineral, crystallinity, gradient in mineral content, the phosphate peak ratio, crosslinking and nature of collagen were assessed (Toledano et al., 2014b) at both intertubular and peritubular dentin.

Relative presence of mineral:

1. *Phosphate* (960 cm^{-1}) *and carbonate* (1070 cm^{-1}) *peaks and areas of their bands.* Peak heights were processed in absorbance units.

2. *Relative mineral concentration* (i.e., mineral-to-matrix ratio): It was inferred from the visible ratio of the intensities of the peaks at 960 cm^{-1} (phosphate) (PO_4^{3-}) and 1003 cm^{-1} (phenyl group), the aromatic ring of phenylalanine residues in collagen, or peaks at 1070 cm^{-1} (carbonate) (CO_3^{2-}) and 1003 cm^{-1}. These indexes concerned with the maximum relative degree of mineralization (Schwartz et al., 2012; Karan et al., 2009). Additionally, peaks at 960 cm^{-1} and 1450 (CH_2) or 1070 cm^{-1} and 1450 can be used (Wang et al., 2009).

Crystallinity: It was evaluated based on the full width at half maximum (Raman-FWHM) of the phosphate band at 960 cm^{-1} and carbonate band at 1070 cm^{-1}. These indexes expressed the crystallographic or relative atomic order, since narrower peaks suggest less structural variation in bond distances and angles (Schwartz et al., 2012). In general, the narrower the spectral peak width is, the higher the degree of mineral crystallinity (Karan et al., 2009).

Gradient in mineral content, or carbonate content of the mineral crystallites: It was assessed as the relationship between the ratio of heights at 1070 cm^{-1} (carbonate) (CO_3^{2-})

to 960 cm^{-1} (phosphate) (PO$_4^{3-}$), indicating carbonate substitution for phosphate (Schwartz et al., 2012).

The organic component of dentin was analyzed examining the following parameters:

Normalization: Phenyl group: The peak at 1003 cm^{-1}, which is assigned to C-C bond in the phenyl group, was used for normalization (Xu and Wang, 2011).

Crosslinking:

1. Pyridinium ring vibration: In the spectra, the peak appeared at 1030/1032.7 cm^{-1}, is assigned to the C-C in pyridinium ring vibration which has a trivalent amino acid crosslinking residue (Daood et al., 2013). The relative intensity of this peak increases after the crosslinking formation (Jastrzebska et al., 2003).

2. Ratio 1660 (amide I)/1690-1701: decreases when mineralization increases.

3. Ratio 1003 (phenyl)/1450 (CH$_2$): arises preceding deposition of HAP (hydroxyapatite) crystals within the structure (Wang et al., 2009).

4. AGEs (advance glycation end products)-pentosidine at 1550 cm^{-1}, interpreted as a marker of the aging process (Sell and Monnier, 1989).

Carboxilic group COO$^-$: The 1415 cm^{-1} band assigned to COO$^-$ stretching mode is related with the formation of ionic bonds with calcium (Strehle et al., 2004).

Lipids: Detection of extra-cellular lipids and phospholipids bands at 1440 and 1465 cm^{-1} reveals the presence of debris of cell membranes, and play an important role during the early stage of hard tissue healing or maturation (Penel et al., 2005).

Nature of collagen:

1. Amide III, CH and Amide I: The peaks at 1246/1270, 1450 and 1655/1667 cm^{-1}, assigned to amide III, CH and amide I, respectively, are sensitive to the molecular conformation of the polypeptide chains (Xu and Wang, 2011;

Jastrzebska et al., 2003). The decrease of amide I peak indicates damage or removal of collagen fibrils (Xu and Wang, 2012).

2. Amide II: from peptide bonds ($\sim$1560 cm^{-1}, N-H bending, and C-N stretching) (Ager et al., 2006).

3. Ratio amide I/amide III concerned the organization of collagen.

4. Ratio amide III /CH$_2$ wagging mode indicates the structural differences (Salehi et al., 2013).

5. Ratio amide I/CH$_2$ indicates altered collagen quality (Salehi et al., 2013).

6. Ratio I/AGEs-Pentosidine, indicative of the glycation reaction *vs* collagen scaffolding (Salehi et al., 2013).

7. 1340 cm^{-1} peak: This signal has been assigned to protein α-helices where intensity is sensitive to molecular orientation (Wang et al., 2009).

3. Results and Discussion

Attained dynamic elastic moduli are displayed in Table 2. Mineral and organic components obtained through Raman analysis are found in Tables 3 and 4. Scanning mode nano-DMA analysis is shown in Figures 1 and 2. 3-D contour map and topography mapping of dentin surfaces are contained in Fig. 3. Spectral Raman analysis are unveiled in Figures 4, 5, 6, and 7. Hierarchical cluster analysis (HCA) is observed in Figure 8.

Table 2. Means and standard deviation (SD) of dynamic elastic moduli: complex modulus (E*) and storage modulus (E') (GPa) of sound and caries affected dentin surfaces with Zn-free and Zn-containing restorations.

		SOUND DENTIN		CAD	
		E*	E'	E*	E'
UNTREATED DENTIN	ID	5.24 (0.35) a1	5.29 (0.25) a1	4.84 (0.71) a1	4.86 (0.28) a2
	PD	10.30 (0.37) A1	10.37 (0.25)A1	10.84 (0.17) A1	10.83 (0.39) A1
TREATED DENTIN — Zn- free restoration	ID	6.71 (0.32) b1	5.08 (0.24) a1	3.51 (0.70) a2	1.56 (0.38) b2
	PD	28.03 (0.33) B1	3.51(0.98) B1	15.57 (0.85) B2	5.43 (1.04) B2
TREATED DENTIN — Zn-containing restoration	ID	13.87 (0.61) c1	5.48 (0.47) a1	27.04 (0.27) b2	8.07 (0.24) c2
	PD	10.82 (0.38) A1	3.73 (0.48) B1	4.24 (0.61) C2	1.53 (0.64) C2
	ITD	5.75 (0.34) 1	2.35 (0.98) 1	2.01 (0.28) 2	0.95 (0.47) 1

Abbreviations: CAD: Caries-affected dentin, ID: intertubular dentin, PD: peritubular dentin, ITD: intratubular dentin, E*: complex modulus, E': Storage modulus. Peritubular, intertubular and intratubular dentin were analyzed separately. Differences in E*or E' between sound and caries affected dentin were indicated with numbers, and differences among experimental treatments with low case letters for intratubular dentin, and capital letters for peritubular dentin.

Table 3a. Mineral components in sound dentin surfaces after the different restorative treatments.

Restoration	Dentin area	Relative Presence of Mineral								FWHM		GMC Ratio C/P
		Phosphate [961]				Carbonate [1070]				Phosphate	Carbonate	
		Peak	Area	RMC	MMR	Peak	Area	RMC	MMR			
Untreated	Peritubular	1114.38	28333.9	22.84	7.06	191.58	5567.22	3.93	1.21	19.39	22.18	0.17
	Intertubular	1343.25	34087.8	14.22	8.12	227.66	9399.43	2.41	1.38	19.35	31.59	0.17
Zn-Free	Peritubular	1058.67	26866	15.61	6.66	194.53	8034.03	2.87	1.22	19.35	31.60	0.18
	Intertubular	1317.11	33424.4	14.83	9.65	238.52	6913.36	2.69	1.75	19.35	22.13	0.18
Zn-Containing	Peritubular	1914.76	42500.85	18.31	6.74	381.83	8350.83	3.65	1.34	17.00	30.92	0.20
	Intertubular	2400.52	51131.7	14.09	9.17	452.32	14099.145	2.65	1.73	16.94	21.84	0.19

RMC: Relative Mineral Concentration between mineral/Phenyl (1003); MMR: Mineral/Matrix (CH_2) Ratio; FWHM- Full-width half-maximum; GMC: Gradient in Mineral Content (carbonate peak/phosphate peak). Peaks positions are expressed in cm^{-1}.

Table 3b. Organic components (normalization, crosslinking, carboxylic group and lipids) on untreated sound dentin surfaces and treated with amalgam after thermocycling.

Restoration	Dentin area	Normalization	Crosslinking						Carboxylic Group	Lipids	
		Phenyl [1003]	Pyrid. [1032]	Ratio [1032/1003]	Ratio [1660/1690]	Ratio phenyl/CH_2 [1003/1450]	AGEs-Pentosidine [1550]		COO⁻ [1415]	[1440]	[1465]
Untreated	Peritubular	48.8	59.65	1.22	1.53	0.31	60.85		98.46	130.1	123.34
	Intertubular	94.46	118.73	1.26	2.13	0.57	73.8		144.28	165.42	156.71
Zn-Free	Peritubular	67.84	85.46	1.26	2.27	0.43	70.55		77.25	125.28	118.05
	Intertubular	88.83	110.02	1.24	0.93	0.65	59.71		82.61	113.49	104.66
Zn-Containing	Peritubular	104.57	237.61	2.27	2.17	0.37	132.1		141.55	356.47	229.34
	Intertubular	170.41	321.84	1.89	0.74	0.65	115.25		152.86	302.69	194.48

Pyrid: Pyridinium; AGEs: advanced glycation end products. Peaks positions are expressed in cm^{-1}.

Table 3c. Organic components (nature and secondary structure of collagen) on untreated sound dentin surfaces and treated with amalgam after thermocycling.

Restoration	Dentin area	A-III [1246-1270]	CH$_2$ [1450]	A-I [1655-1667]	A-II [1560]	Ratio A-I/ A-III	Ratio A-III/ CH$_2$	Ratio A-I/ CH$_2$	Ratio A-III/ AGEs-Pentosidine	Ratio A-I/ AGEs-Pentosidine	α-helices [1340]
Untreated	Peritubular	201.52	157.85	73.79	51.05	0.37	1.28	0.47	3.31	1.21	116.4
	Intertubular	225.04	165.42	92.22	73.8	0.41	1.36	0.56	3.05	1.25	134.04
Zn-Free	Peritubular	196.39	159	95.81	60.34	0.49	1.24	0.60	2.78	1.36	105.1
	Intertubular	200.24	136.52	222.21	66.28	1.11	1.47	1.63	3.35	3.72	77.59
Zn-Containing	Peritubular	753.35	284.11	264.02	81.97	0.35	2.65	0.93	5.70	2.00	287.2
	Intertubular	698.2	261.77	642.25	74.81	0.92	2.67	2.45	6.06	5.57	211.46

A-III: Amide III; A-I: Amide I; A-II: Amide II; AGEs: advanced glycation end products. Peaks positions are expressed in cm^{-1}.

Table 4a. Mineral components on untreated caries-affected dentin surfaces and treated with amalgam after thermocycling.

Restoration	Dentin area	Relative Presence of Mineral								FWHM		GMC Ratio C/P
		Phosphate [961]				Carbonate [1070]						
		Peak	Area	RMC	MMR	Peak	Area	RMC	MMR	Phosphate	Carbonate	
Untreated	Peritubular	964.09	27648.9	9.69	8.34	207.86	7731.19	2.09	1.80	22.58	28.44	0.22
	Intertubular	763.19	19367.5	20.68	7.84	106.19	5325	2.88	1.09	19.35	38.44	0.14
Zn-Free	Peritubular	1223.32	31044.3	5.22	11.60	321.27	25146	1.37	3.05	19.35	60.35	0.26
	Intertubular	979.86	24866	5.73	7.17	261.29	22566	1.53	1.91	19.35	66.70	0.27
Zn-Containing	Peritubular	2143.15	34572	4.63	17.09	590.83	12221.9	1.28	4.71	19.34	60.12	0.28
	Intertubular	1834.14	23461.05	5.47	12.11	562.32	5647.44	1.68	3.71	19.35	65.91	0.31

RMC: Relative Mineral Concentration between mineral/Phenyl (1003); MMR: Mineral/Matrix (CH_2) Ratio; FWHM- Full-width half-maximum; GMC: Gradient in Mineral Content (carbonate peak/phosphate peak). Peaks positions are expressed in cm^{-1}.

Table 4b. Organic components (normalization, crosslinking, carboxylic group and lipids) on untreated caries-affected dentin surfaces and treated with amalgam after thermocycling.

Restoration	Dentin area	Normalization	Crosslinking					Carboxylic Group COO⁻ [1415]	Lipids	
		Phenyl [1003]	Pyrid. [1032]	Ratio [1032/1003]	Ratio [1660/1690]	Ratio phenyl/CH_2 [1003/1450]	AGEs-Pentosidine [1550]		[1440]	[1465]
Untreated	Peritubular	99.51	113.81	1.14	9.53	0.86	165.49	174.47	215.68	206.76
	Intertubular	36.9	38.09	1.03	0.76	0.38	92.53	95.09	103.62	109.72
Zn-Free	Peritubular	234.13	105.80	0.45	0.80	2.22	87.07	57.87	89.91	92.18
	Intertubular	170.99	86.49	0.51	0.78	1.25	108.67	93.6	139.84	75.85
Zn-Containing	Peritubular	463.24	194.52	0.42	0.86	3.69	149.62	70.03	113.65	119.22
	Intertubular	335.18	140.21	0.42	0.82	2.21	187.23	127.74	152.63	91.88

Pyrid: Pyridinium; AGEs: advanced glycation end products. Peaks positions are expressed in cm^{-1}.

Table 4c. Organic components (nature and secondary structure of collagen) on untreated caries-affected dentin surfaces and treated with amalgam after thermocycling.

Restoration	Dentin area	A-III [1246-1270]	CH$_2$ [1450]	A-I [1655-1667]	A-II [1560]	Ratio A-I/ A-III	Ratio A-III/ CH$_2$	Ratio A-I/ CH$_2$	Ratio A-III/ AGEs-Pentosidine	Ratio A-I/ AGEs-Pentosidine	α-helices [1340]
Untreated	Peritubular	290.86	115.66	427.61	148.68	1.47	2.51	3.70	1.76	2.58	164.39
	Intertubular	183.61	97.38	239.1	122.79	1.30	1.89	2.46	1.98	2.58	133.04
Zn-Free	Peritubular	270.6	105.5	594.06	79.29	2.20	2.56	5.63	3.11	6.82	150.94
	Intertubular	247.96	136.68	401.61	69.22	1.62	1.81	2.94	2.28	3.70	167.56
Zn-Containing	Peritubular	301.7	125.42	632.2	90.15	2.10	2.41	5.04	2.02	4.23	35.94
	Intertubular	273.53	151.43	473.81	82.43	1.73	1.81	3.13	1.46	2.53	77.21

A-III: Amide III; A-I: Amide I; A-II: Amide II; AGEs: advanced glycation end products. Peaks positions are expressed in cm^{-1}.

Figure 1
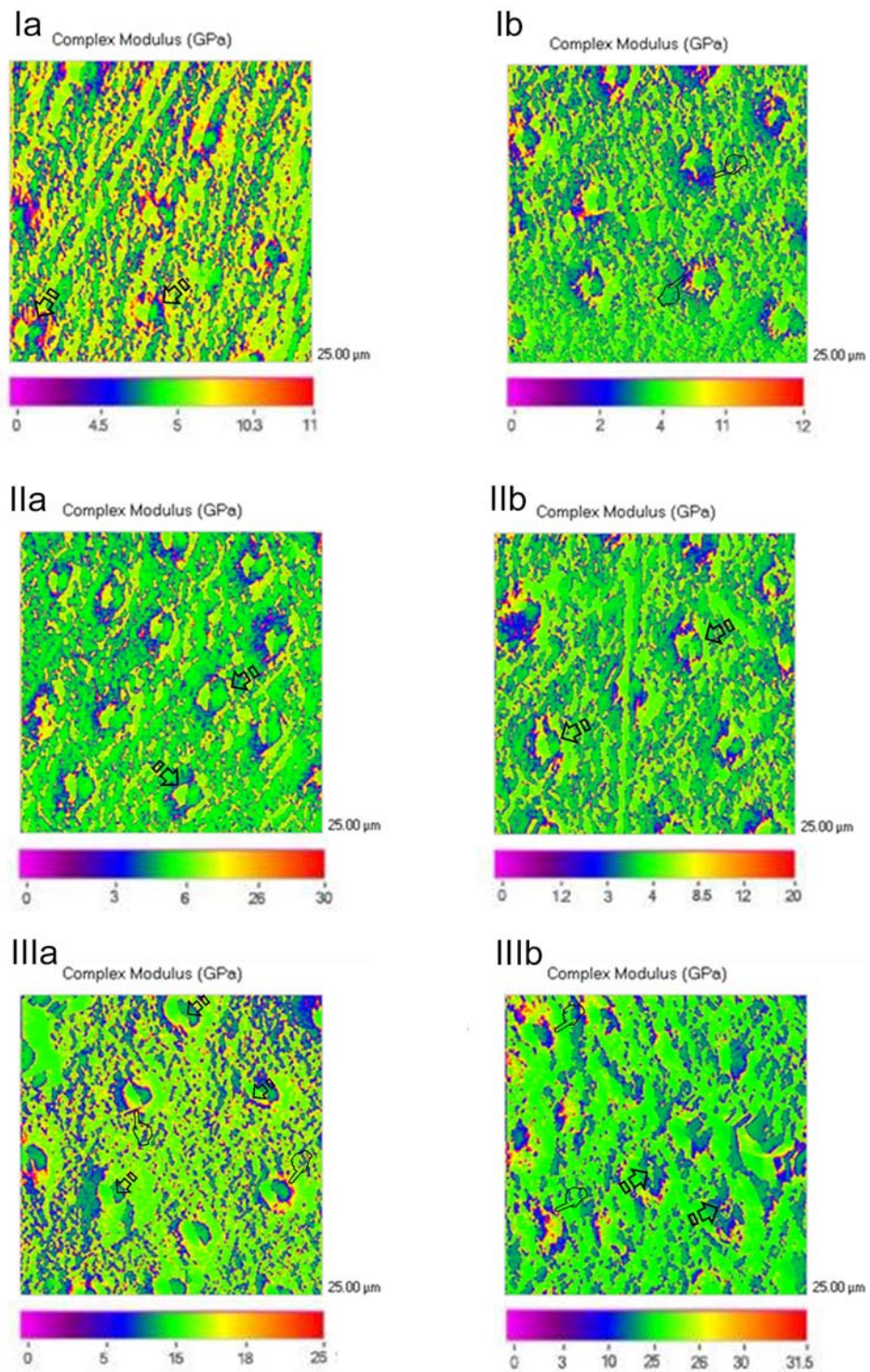
Figure 1: Scanning mode nano-DMA analysis of the map of the complex modulus at the untreated dentin surface (I), dentin surface after removal of Zn-free amalgam restorations (II), and dentin surface after removal of Zn-containing amalgam

restorations (III); (a) sound dentin, (b) caries-affected dentin. In the color scheme shown, the darker color corresponds to lower values of the locally measured complex modulus E^*. Discontinuous red collar point out areas of maximum E^* (arrows) (I·a). Closed loops in blue and yellow to red traces signalize regions of maximum E^* (pointers) (Ib). Septum-split spheres characterized the regions of higher E^* (arrows) in sound dentin (IIa). Homogeneous spheres of higher complex modulus gave rise in caries-affected dentin substratum (arrows) (IIb). Greener zones (arrows) within the redder collar of higher E^* values (pointers) suggest intratubular precipitation of crystals (IIIa). Irregular blue circles spread out in the scan surface (arrows) and most of them appeared framed by a collar of multiple red spots (pointers) (IIIb).

Figure 2
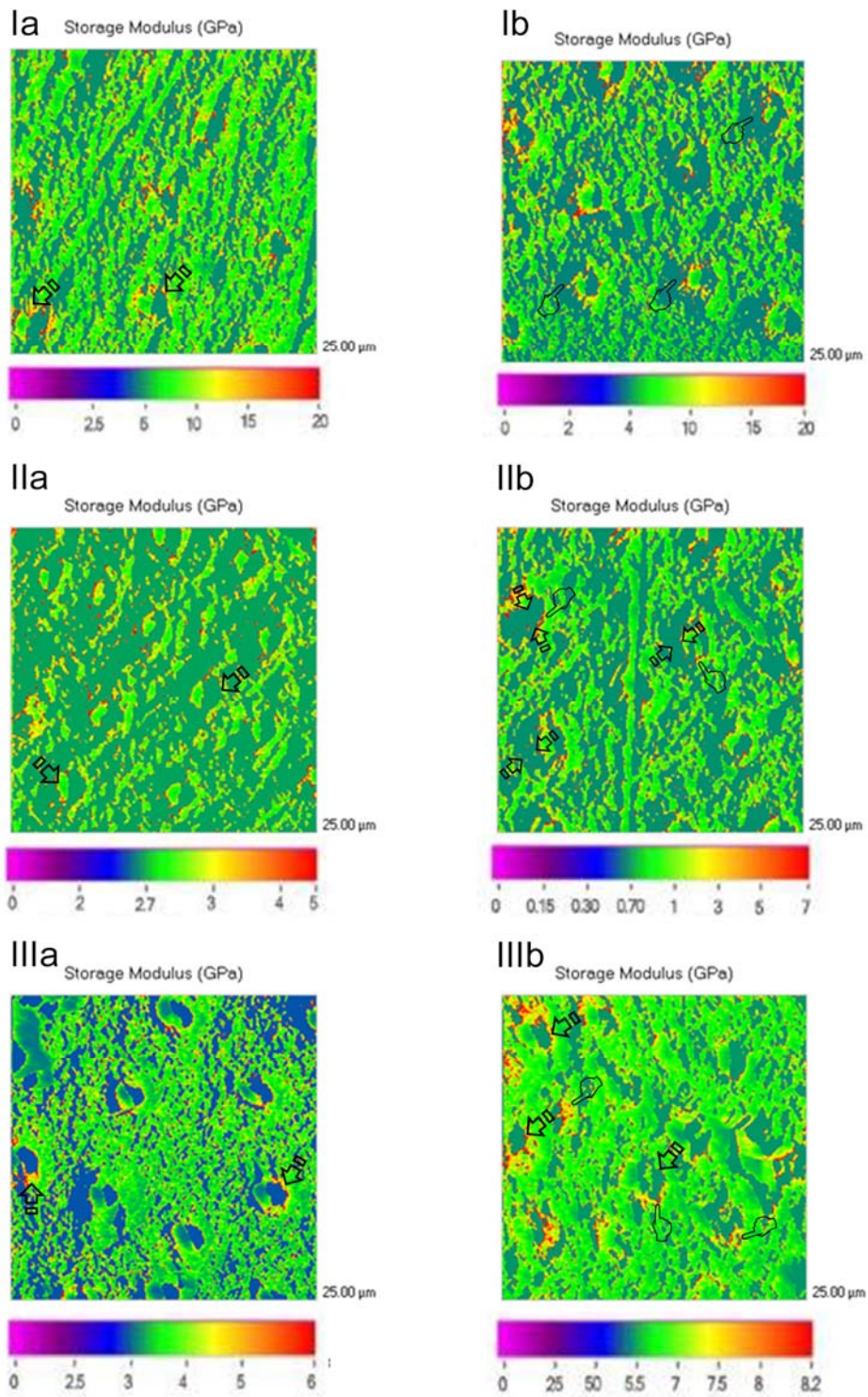
Figure 2: Scanning mode nano-DMA analysis of the map of the storage modulus at the untreated dentin surface (I), dentin surface after removal of Zn-free amalgam restorations (II), and dentin surface after removal of Zn-containing amalgam

restorations (III); (a) sound dentin, (b) caries-affected dentin. In the color scheme shown, the darker color corresponds to lower values of the locally measured storage modulus E'. Non-regular yellow to red collar point out areas of maximum E' (arrows) (Ia). Rings of a sharp yellow to red (inner) and wide blue (outer) signalize maximum E' (pointers) (Ib). Punctual red signals surrounded by blue to green regions were adverted in the scan (arrows) (IIa). Wider circles (~1-3 μm thick) (between arrows) limited by areas of higher E' (pointer) appeared in the modulus map (IIb). Clear signals of energy stored at peritubular dentin are shown (arrows) (IIIa). IIIb shows different zones (arrows) with lower storage modulus surrounded by other areas with high storage modulus (pointers), where the excess energy may be dissipated through cracking the tissue.

Figure 3
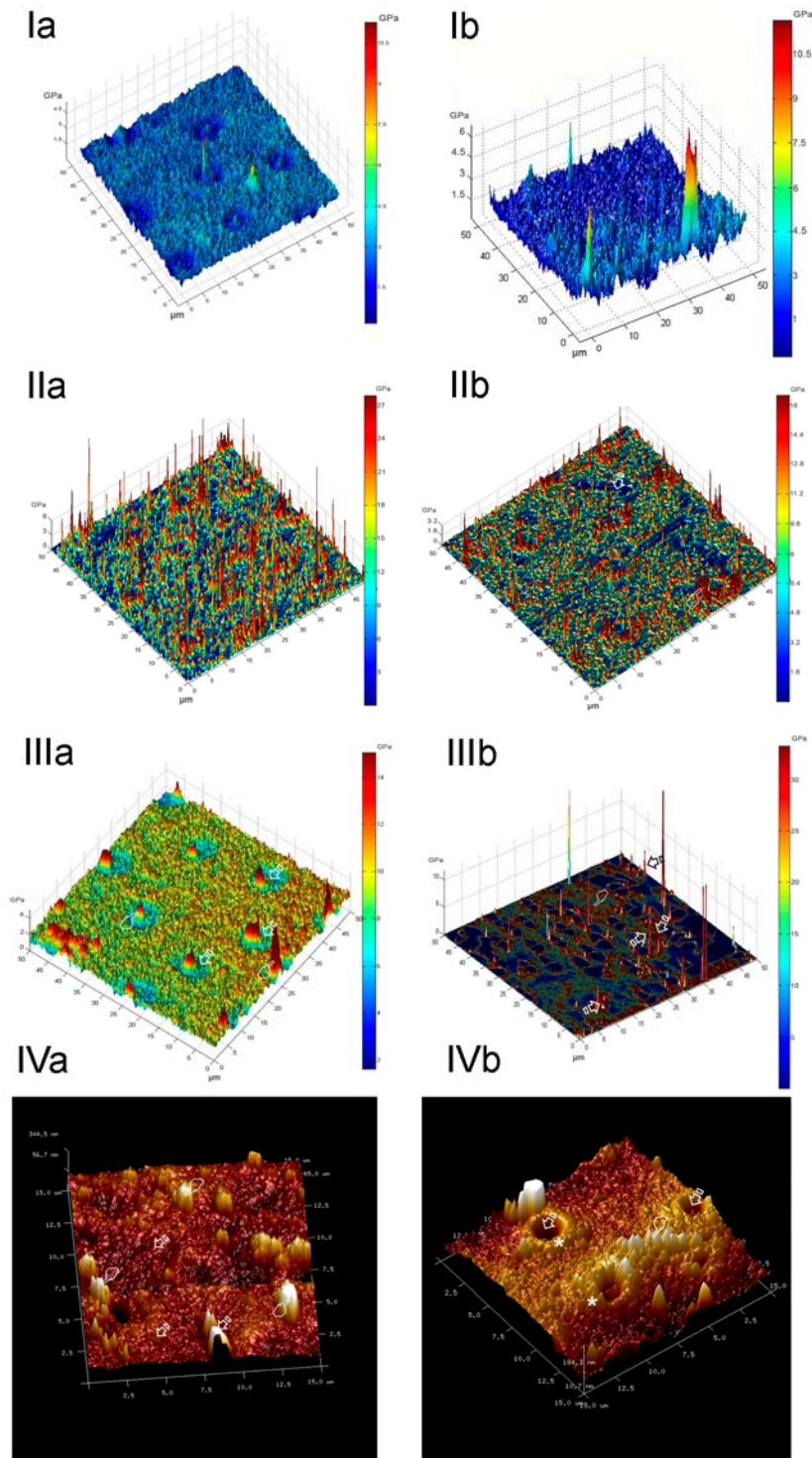
Figure 3: 3-D contour map of the complex modulus (E^*) distribution in untreated dentin surface (I), dentin surface after removal of Zn-free amalgam restorations (II),

dentin surface after removal of Zn-containing amalgam restorations (III) and topography mappings obtained by AFM after Zn-containing removal restoration (IV); (a) sound dentin, (b) caries-affected dentin. In the color scheme shown (I, II and III), the darker color corresponds to lower values of the locally measured complex modulus E^*. Ia shows multiple blue moles and some finest peaks of higher intensities, localized at peritubular areas. Ib exhibits some acute peaks of higher intensities at the bottom of the map. IIa permits to observe the highest complex modulus that attained at the present study. IIb shows that E* ranges from 15.57 (peritubular dentin) (pointer) to 3.51 (intertubular dentin) (arrow) GPa. IIIa unveils the E^* values of the radial mineral formations which anchored the intratubular nucleated minerals to the peritubular dentin, "bridging" both mineralized dentin structures (arrows). IIIb permits to observe the highest complex modulus (27.04 GPa) that attained at intertubular dentin (arrows), in the present study. Resistance to deformation was adverted in the majority of the intratubular spaces in sound dentin (IIIa), or in some of them (IIIb) (pointers). IVa unveils mineralized tubular occlusion (arrows), and rod-like new mineral formations (pointer) covering the sound dentin surface. IVb exhibits a map of empty dentin tubules and formations of rod-like new mineral or stick-slip formations (pointers) covering the caries-affected dentin surface; strongly mineralized peritubular dentin, forming clear and robust rings, may be adverted (asterisks). In order to facilitate the observation of different morphological features on dentin surfaces, AFM images have been tilted, so surfaces look rougher than they really are.

Figure 4
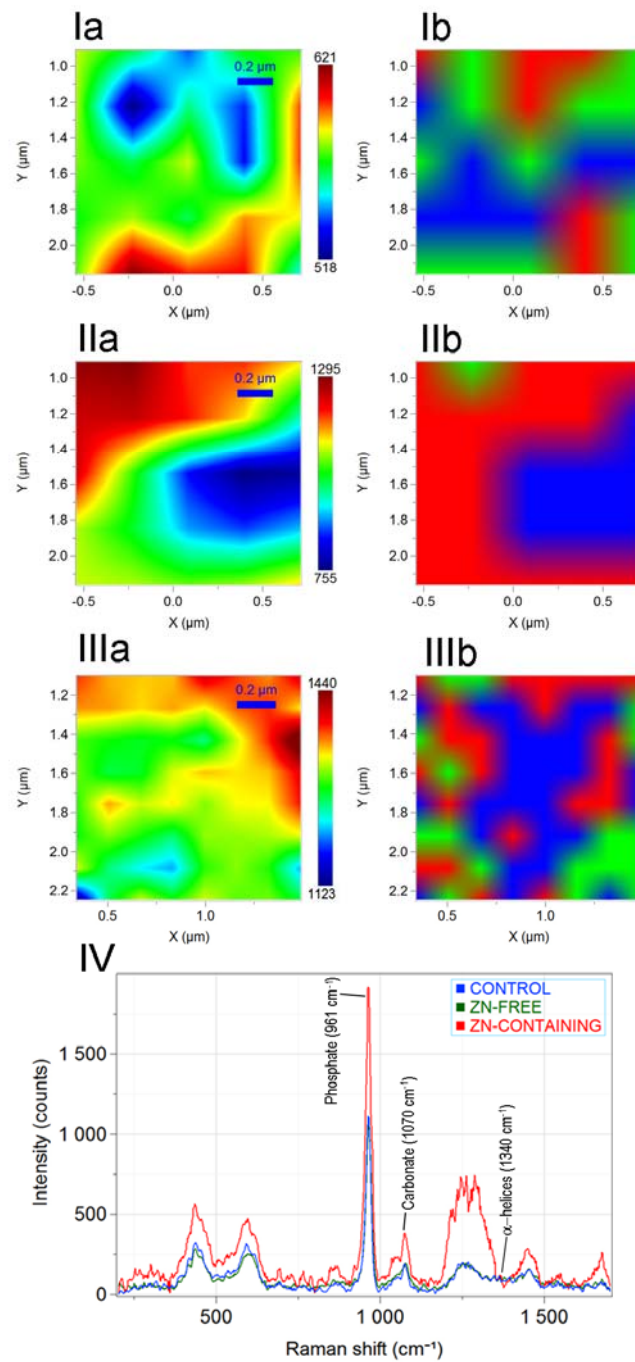
Figure 4: RAMAN analysis of peritubular sound dentin; control (I), after Zn-free amalgam removal (II), after Zn-containing amalgam removal (III) restorations, characteristic single-point Raman spectra of the tested surfaces (IV). 2D micro-Raman map of 961 cm⁻¹ intensities at the dentin surface (a). At the 2D micro-Raman, blue

represents the lowest peak intensity, while the red represents the highest. K-means clustering (KMC) map of the Raman profile of the same samples (b).

Figure 5
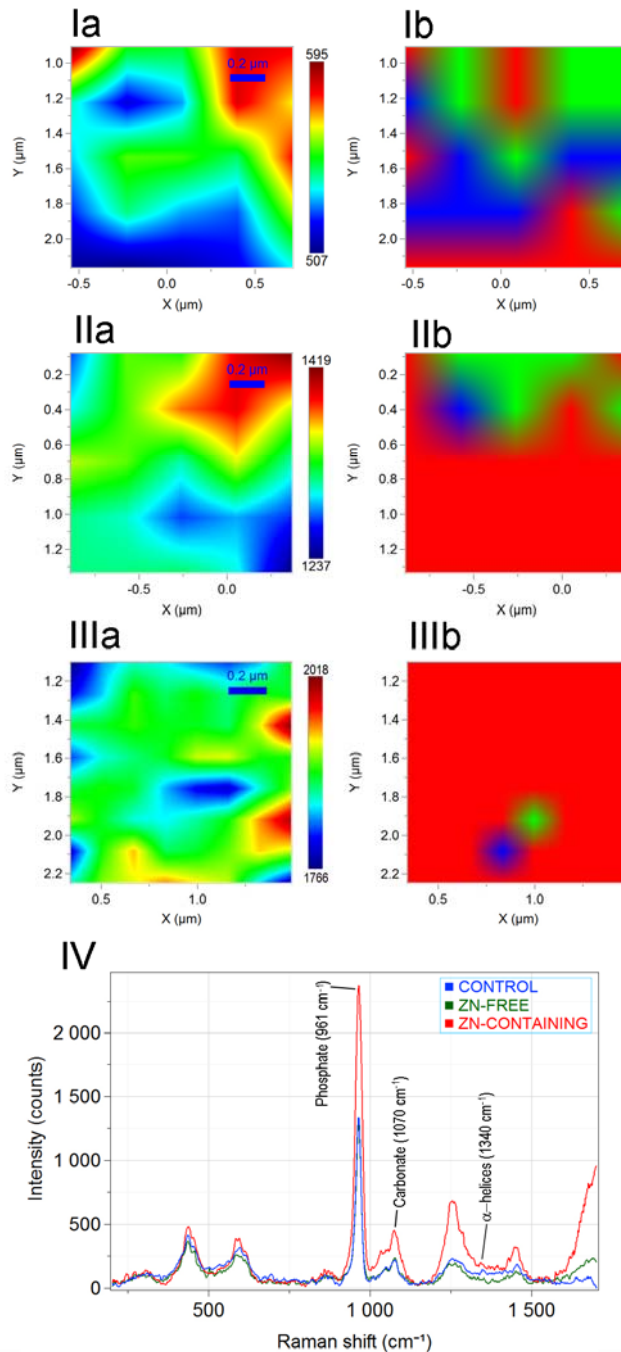
Figure 5: RAMAN analysis of intertubular sound dentin; control (I), after Zn-free amalgam removal (II), after Zn-containing amalgam removal (III) restorations, characteristic single-point Raman spectra of the tested surfaces (IV). 3D micro-Raman

map of 961 cm^{-1} intensities at the dentin surface (a). At the 2D micro-Raman, blue represents the lowest peak intensity, while the red represents the highest. K-means clustering (KMC) map of the Raman profile of the same samples (b).

Figure 6
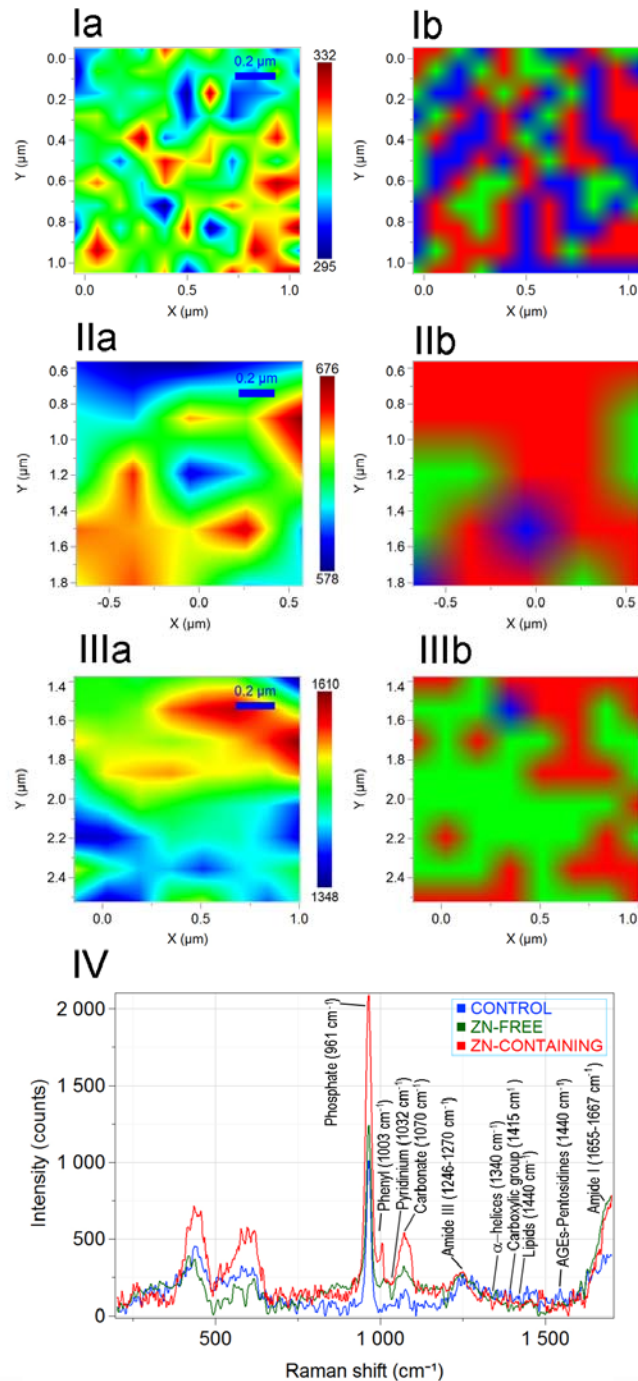
Figure 6: RAMAN analysis of peritubular caries-affected dentin; control (I), after Zn-free amalgam removal (II), after Zn-containing amalgam removal (III) restorations,

characteristic single-point Raman spectra of the tested surfaces (IV). 2D micro-Raman map of 961 cm^{-1} intensities at the dentin surface (a). At the 2D micro-Raman, blue represents the lowest peak intensity, while the red represents the highest. K-means clustering (KMC) map of the Raman profile of the same samples (b).

Figure 7
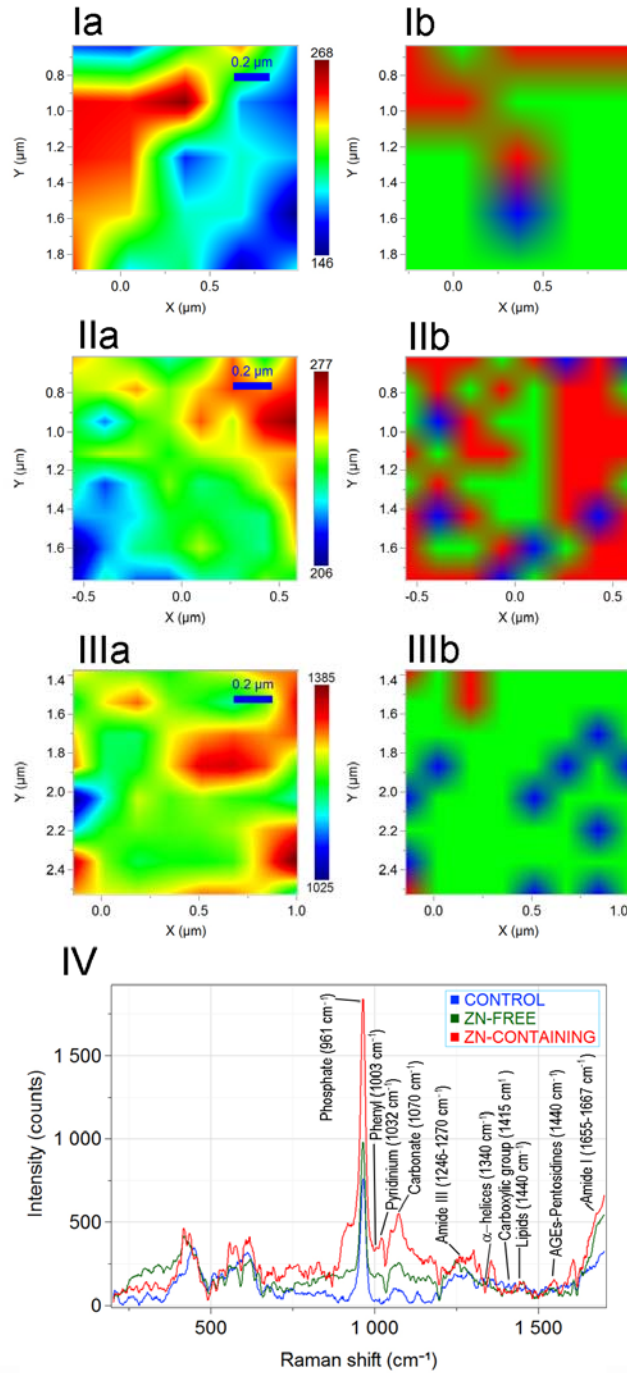
Figure 7: RAMAN analysis of intertubular caries-affected dentin; control (I), after Zn-free amalgam removal (II), after Zn-containing amalgam removal (III) restorations, characteristic single-point Raman spectra of the tested surfaces (IV). 2D micro-Raman map of 961 cm^{-1} intensities at the dentin surface (a). At the 2D micro-Raman, blue represents the lowest peak intensity, while the red represents the highest. K-means clustering (KMC) map of the Raman profile of the same samples (b).

Figure 8
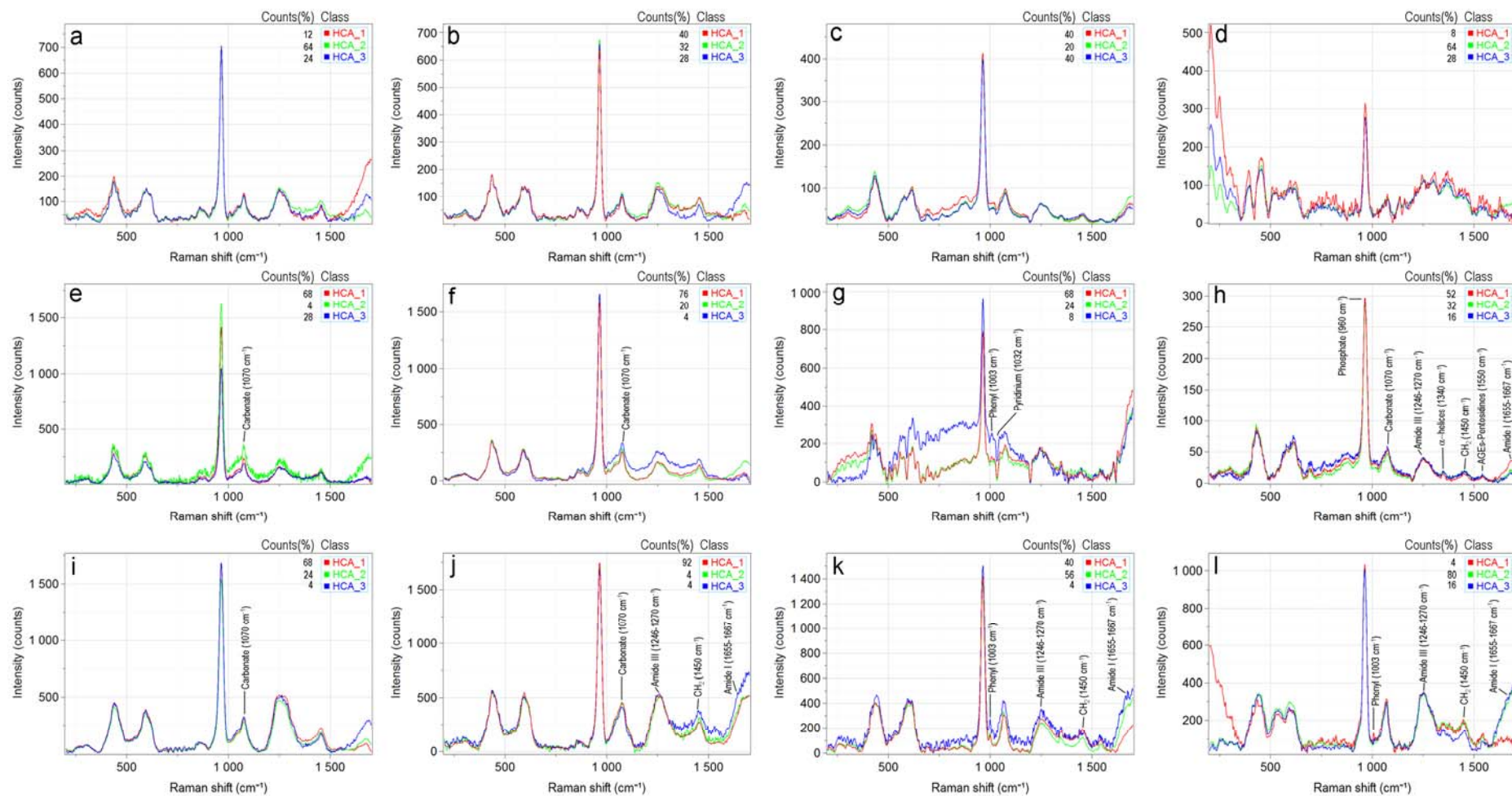
Figure 8: Hierarchical cluster analysis (HCA) results of control dentin, sound peritubular (a) and intertubular (b) locations; caries-affected dentin, peritubular (c) and intertubular (d) locations. HCA results of peritubular (e) and intertubular (f) sound dentin, and peritubular (g) and intertubular (h) caries-affected dentin after Zn-free amalgam removal. HCA results of peritubular (i) and intertubular (j) sound dentin, and peritubular (k) and intertubular (l) caries-affected dentin after Zn-containing amalgam removal.

The lower complex and storage modulus obtained at the peritubular dentin, in comparison with the intertubular dentin in caries-affected dentin treated with Zn-containing restoration indicates the clear augmentation of the stress concentration within the peritubular cuff. This may dissipate through cracking the dentin substrate altering the transfer of energy, with implications for dentin remineralization and remodeling.

The present research sought to gain insights into the role of different Zn-free or Zn-containing restoration leading to nanoscopic dynamic mechanical recovery or improvement. It also deals with remineralization of partially demineralized dentin in caries-affected dentin substrata, at peritubular (PD) and intertubular dentin (ID) locations, after a thermo-cycling challenge. Scanning of these two selected regions of interest enabled identification of both PD and ID in the property maps. Thus, it revealed that there is heterogeneity in the mechanical property distribution of those regions. How, structurally, the dentin interface dissipates and stores energy is likely to be related to the stress transfer mechanism during the thermo-cycling procedure. Due to the increase in mineral content at the interface after thermo-cycling (Toledano et al., 2014c) changes to the elastic mechanical behavior are not unexpected. This increase became, in caries-affected dentin samples restored with Zn-free restorations, associated to higher values of relative presence of minerals concerning both the phosphate (PO_4^{3-}) (961 cm^{-1}) and the carbonate (CO_3^{2-}) (1070 cm^{-1}) peaks, at both peritubular and intertubular substrata after thermo-cycling, in comparison with samples not treated nor thermo-cycled (Table 4a).

3.1. Raman spectroscopy and cluster analysis of dentin surfaces

Single-point spectroscopy analysis also confirmed that at peritubular dentin of caries-affected dentin surfaces, thermo-cycling promoted and increase of ~1.27 and 1.12 fold

at both peak and area of the PO_4^{3-} group (Table 4a) (Fig. 6·IV). Besides, at intertubular dentin this augmentations was ~1.28 fold at both peak and area (Fig. 7·IV), when dentin was treated with Zn-free restoration and compared with the untreated group. The Raman phosphate peak at $961 cm^{-1}$ characterizes tetrahedral PO_4 group (P-O bond) within hydroxylapatite. Monitoring the intensity of this peak has been used to assess the potential increase in phosphate content (Milly et al., 2014). Similar trend was followed by the CO_3^{2-} group, which gained an approximately 1.55 and 3.25 fold of intensity at both peak and area at peritubular dentin, and ~2.46 and 4.24 fold at both peak and area, at intertubular dentin (Table 4a) (Fig. 7·IV). These indexes concerned with the maximum relative degree of mineralization (Schwartz et al., 2012; Karan et al., 2009). Therefore, the univariate intensity map of the Raman shift values of $961 cm^{-1}$ at peritubular dentin displayed higher intensities of the phosphate peak in caries-affected dentin than in the sound specimens after using Zn-free amalgam restorations submitted to thermo-cycling (Tables 3a, 4a). This indicated the formation of new mineral in the previous partially demineralized dentin regions. The single-point spectroscopy is not sufficient to accurately describe the chemical composition of dentin. Instead, the addition of bi-dimensional (2D) or unsupervised data analysis technique-based spatial information is needed (Krafft et al., 2009; Timlin et al., 2000). These data were confirmed through our 2D-micro Raman analysis (Figs. 6·IIa, 7·IIa), as the phosphate peak ($961 cm^{-1}$) increased at both dentin surfaces (Figs. 6·IV, 7·IV). Furthermore, this mineralized area was visible in the region at about -0.75/0.25 µm in the X-direction with 1.2/1.8 µm in the Y-direction, at peritubular dentin (Fig. 6·IIa). At intertubular dentin, this phosphate-rich region extended from approximately 0.12/0.65 µm (X) to 1.2/0.8 µm (Y) (Fig. 7·IIa).

When Zn-containing restorations were used to restore sound dentin, values of the relative presence of minerals concerning the phosphate (PO_4^{3-}) (961 cm^{-1}) peak, increased ~1.80 and 1.71 fold higher than when Zn-free restorations were used or untreated samples were analyzed, respectively, at peritubular dentin. Similarly, the presence of Zn in the chemical formulation of the restoration promoted an increased of the phosphate peak ~1.82 and 1.79 fold, at intertubular dentin, when compared with both Zn-free restoration and control groups, respectively (Table 3a). These differences became bigger when Zn-containing restorations were employed in caries-affected dentin substrata, as the phosphate augmented ~1.75 and 2.22 fold at peritubular dentin, and ~1.87 and 2.40 fold at intertubular dentin. The carbonate peak also augmented in caries-affected dentin substrata when Zn-containing restorations were used, ~1.83 and 2.84 fold at peritubular dentin, in samples treated with Zn-free or untreated, respectively. It also increased ~2.15 and 5.29 fold at intertubular dentin, in the same groups (Table 4a). The Raman observations permitted to resolve that at caries-affected dentin surfaces treated with Zn-containing restorations the highest peaks at 961 cm^{-1} intensities matched those hydroxylapatite, the same phase which was observed after Raman spectra of the principal component (Figs. 6·IV, 7·IV). 2D-micro Raman analysis permitted to observe the augmentation of the phosphate peak in the region of ~0.3-1.0 μm in the X-direction with 1.0-1.5 μm in the Y-direction, at peritubular dentin of caries-affected dentin (Fig. 6·IIIa). At intertubular dentin, this phosphate-rich region extended from approximately 0.25-1.0 μm (X) to 2.5-2.2 and 2.0-1.4 μm (Y) (Fig. 7·IIIa). The meaning of the three clusters from a chemical point of view is that we have three distinct forms of mineralized dentin attending to detected differences in some peak intensities.

Raman images were produced by PCA (principal components analysis) and HCA (hierarchical cluster analysis) in the spectral range between 200 and 1700 cm^{-1} in

order to automatically distinguish chemical differences components at microstructural levels. Thus, the corresponding HCA Raman images showed an homogenizing effect of the main three clusters of the peritubular dentin, after treating caries-affected dentin surfaces with Zn-free restorations, with a good description of the dentin composition (Figs. 6·Ib, 6·IIb). HCA results reflected the chemical differences and the spatial distribution of the main spectra. Two out the three distinguishable clusters almost overlapped (red/HCA_1 and green/HCA_2), and the intensity peak corresponding to the phosphate group increased higher in the blue one (HCA_3) (Fig. 8g). At intertubular caries-affected dentin, crystallinity did not change after restoring with Zn-free nor with Zn-containing amalgams thermo-cycled (Table 4a), but augmented at sound dentin when Zn-containing restorations were applied (16.94) (Table 3a). FWHM augmented at both peritubular dentin and intertubular dentin (~1.89 fold) in the group of B-type carbonate (CO_3^{2-}) (1070 cm^{-1}) when caries-affected dentin was restored, regardless the presence of Zn (Table 4a), and therefore crystallinity concerning the carbonate v_1 peaks diminished. On the contrary, carbonate crystallinity increased at intertubular dentin in sound dentin (Table 3a). Carbonated apatite is a precursor of hydroxyapatite, as it is unstable. Furthermore, in the present study it resulted less mature by default of the poor crystallinity in caries-affected dentin (Table 4a). It is speculated that the amorphous status of the resultant carbonated apatite confers higher energy state to the substrate, hindering the atomic motion and challenging the reorganization toward structures more crystalline (Lee et al., 2002a).

Raman analysis also showed that the intensity of the peak corresponding to normalization (1003 cm^{-1}) increased ~2.35 (peritubular dentin) and 4.63 (intertubular dentin) fold in caries-affected dentin restored with Zn-free amalgams, and almost became double after using Zn-containing restorations, after thermo-cycling (Table 4b).

An increase in the protein-dependent spectral signal at phenylalanine preceded the appearance of hydroxyapatite crystals (Wang et al., 2009). Raman spectra of the principal components confirmed this augmentation at the 1003 cm^{-1} bands of both peritubular and intertubular caries-affected dentin surfaces (Figs. 6·IV, 7·IV). At intertubular dentin, HCA images appeared with disaggregated granular-shaped clusters (Fig. 7·IIb), but HCA results showed overlapped spectra (Fig. 8h). The spectra corresponding to these intertubular dentin are very different from peritubular clusters. They are characterized by intense bands located especially around 960, 1070, 1260, 1340, 1450, 1560 and 1660 cm^{-1} (Fig. 8h) at intertubular dentin, and a prominent band at 1003 and inverted peak at 1032 cm^{-1} (Fig. 8g), at peritubular dentin. These Raman signals correspond to augmentation of the relative presence of minerals, improvement of nature and secondary structure of collagen, and favorable molecular orientation (Xu and Wang, 2012; Wang et al., 2009; Schwartz et al., 2012). The high intensity band of proteins (phenyl group) (1003 cm^{-1}) corresponded with advanced normalization (Xu and Wang, 2011) at peritubular dentin, and the decrease of 1032 cm^{-1}, with a reduction in crosslinking capability (Jastrzebska et al., 2003) of the same dentin (Fig. 8g). Moreover, the fact that these two groups (HCA_1 and HCA_2 + HCA_3) (Fig. 8g) are much more dispersed than at intertubular dentin (Fig. 8h), confirms the relative high level of heterogeneity of these type of dentin, mostly due to a different level of maturation of each measured cluster (Vanna et al., 2015). The HCA_1, the first principal component (loadings in Figs. 6·IIb, 8g), which described 68% of the variance of the entire dataset, mainly defines differences between these two principal grouped clusters. The intensity bands around 1003 cm^{-1} (phenyl-alanine) and 1660 cm^{-1} (amide I band), assigned to proteins, and the band around 1450 cm^{-1} (C-H deformation bands) (generally assigned to proteins, lipids and carbohydrates) are in accordance with the

immature stage (Vanna et al., 2015) of dentin. On the other hand, HCA_3 (representing 8% of the spectral variance) does not describe significant variations related to the spectra between ~1200-1700 cm^{-1}, but clearly discriminated from 200-1200 cm^{-1}, except at the PO$_4$ band (phosphate), which overlapped (Figs. 5·IIb, 8g).

Peritubular dentin consists of a highly mineralized zone, ~ 1 μm thick (Balooch et al., 2004), and a protein matrix. This organic content is a mixture of acidic phosphoproteins (140-170 KDa) that function much like phosphophorins, but have a different aminoacid composition (Weiner et al., 1999) that is free of hydroxyproline. The major proteins of peritubular dentin seem to be developmental proteins, rather than structural proteins, and they probably serve to control calcium binding and crystal growth (Ryou et al., 2015). Collagen crosslinking is affected by tissue maturation as well as degree of mineralization, providing information about the structure and molecular interactions of complexes biomolecules (Xu and Wang, 2011; Saito et al., 2006). At peritubular dentin, crosslinking of collagen diminished in caries-affected dentin substrate restored with Zn-free amalgam after thermo-cycling. Hence, the majority of indexes, *e.g.,* pyridinium (1032 cm^{-1}), ratio 1660 cm^{-1}/1690 cm^{-1} and AGEs-Pentosidine (1550 cm^{-1}) confirmed this drop after cycling (Fig. 7·IV). When Zn-containing restorations were used on caries-affected dentin substrate, crosslinking augmented, in general, at both peritubular and intertubular dentin, when compared with the control group (Table 4b). They became associated with the increment in the relative presence of minerals (Table 4a). Collagen crosslinking improved mechanical strength and stability of dentin collagen (Xu and Wang, 2012). It permitted the growing of minerals within the demineralized dentin, as three-dimensional structures supporting effective mineralization may be created between intrafibrillar collagen molecules via the formation of specific crosslinking that guide proper mineralization (Saito et al., 2013).

When Zn-free amalgams were used in caries-affected dentin substrata, the intensity peak of the carboxylic group (COO$^-$) at 1415cm^{-1} decreased ~3.01 and ~1.01 fold at peritubular and intertubular dentin, respectively, and resulted lower than that obtained when Zn-containing restorations were used (Table 4b). This might suggest the formation and further increase of ionic bond with calcium (Coutinho et al., 2007) when carious dentin was restored in presence of zinc. Band shifts corresponding to lipids at 1465 cm^{-1} diminished at peritubular dentin and intertubular dentin, but augmented (~1.35 fold) at 1440 cm^{-1}, at intertubular dentin, in samples of caries-affected dentin restored with Zn-free amalgams, and ~1.47 fold with Zn-containing restorations, thermo-cycled (Table 4b). Those spectral changes observed in the lipid bands confirm the presence of tissue healing and maturation (Penel et al., 2005).

From our modeling of HCA spectral data, it may be observed the drastic increase of the band at 1003 cm^{-1} (proteins) at both peritubular and intertubular dentin, after using Zn-containing restorations in caries-affected dentin (Figs. 8k, 8l). At peritubular dentin, three distinguishable different groups were clustered in contiguous traces of the scatter plots, according to similar conditions of maturing (Vanna et al., 2015). Hence, these traces were accompanied by prominent intensities at 1260, 1450 and 1660 cm^{-1}, more intense in the HCA_3, which showed the lowest variance among groups (4%) (Fig. 8k). Those spectra confirmed the immature stage of the peritubular dentin, though HCA_1, which contributed with 40% of the spectral variance, attained lower intensity peak at 1660 cm^{-1} (amide I), resulting in a heterogeneous (Vanna et al., 2015) dentin substrate. This immaturity was confirmed by the decrease, ~1.9 fold, of the intensity peak corresponding to lipids at 1440 cm^{-1}. This drop was even more pronounced when Zn-free amalgams were used in the carious dentin, which diminished ~1.9 fold (Table 4b), denoting some delay in the process of healing and maturation

(Penel et al., 2005). The spectra corresponding to intertubular dentin (Fig. 8l), in specimens of caries-affected dentin, treated with Zn-containing restorations are very different from peritubular dentin as only one cluster (HCA_2, in green) represented 80% of variance. The lowest intensity peak corresponding to the Amide I resulted associated to HCA_1, which represented the 4% of counts of the whole variance. The most prominent characteristic of HCA related to sound dentin specimens treated with Zn-containing amalgams was the 92% contribution of HCA_1 in the whole variance of the spectra (Fig. 8j), conferring high homogeneity with low dispersion to the mature (Vanna et al., 2015) dentin substrate. Note the high intensity peaks at 1260, 1450 and 1660 cm^{-1}, that indicates advance maturation in comparison to the intertubular sound dentin treated with Zn-free restorations (Fig .8f). It also should be highlighted the height and area of the carbonate peak (1072 cm^{-1}), signifying the increase of carbonate apatite, precursor of the hydroxyapatite (Lee et al., 2002b), more prominent at intertubular dentin (Fig. 8j) than at peritubular dentin (Fig. 8i), but both bigger than in sound dentin treated with Zn-free amalgams (Figs. 8e, 8f). As a result of the previous outcomes that have been shown and discussed, the null hypothesis that there are no differences in the mechanical properties and chemistry of inter- and peritubular dentin of sound and caries-affected substrata after removal of Zn-free *vs* -containing restorations submitted to thermo-cycling, must be rejected.

At both peritubular and intertubular dentin, ratios concerning nature and secondary structure of collagen in samples of caries-affected dentin restored with Zn-free amalgams and thermo-cycled increased their intensities, except at A-III/CH_2 (Table 4c); both A-III and CH_2 peaks also increased, but CH_2 proportionally bigger, resulting in lower ratio, at intertubular dentin (Table 4c) (Fig. 7·IV). When Zn-containing restorations were used, those values increased, in general, except in A-II, ratio A-

III/CH$_2$ and ratio A-III/AGEs-pentosidine, at intertubular dentin. All of these ratios and indexes are expected to increase when mineralization occurs (Toledano et al., 2014a), preceding the appearance of phosphate stretching peak at 960 cm^{-1} (Figs. 6·IV, 7·IV); this purports that nucleation is a multistep process involving both protein and mineral transition, suggesting a temporally synchronized proceeding (Wang and Yao, 2010). Sound dentin performed similar in the same conditions (Table 3c). Ratio A-I/AGEs-Pentosidine, indicative of the glycation reaction *vs* collagen scaffolding (Salehi et al., 2003) increased in samples of sound and caries-affected dentin restored with Zn-free and -containing amalgams, and thermo-cycled. Glycation promoted formation of cross-links between molecules, causing an increase in the area of the extracellular matrix, resulting in increased stiffness (Goldin et al., 2006). Through scaffolding, local environmental conditions for guiding and assisting the generation of natural extracellular matrix and mineral deposition are provided and so mechanical integrity and functionality (Zhang et al., 2013). Band shifts corresponding to α-helices dropped (~1.10 and 1.73 fold at peritubular and intertubular dentin, respectively) in samples of sound dentin restored with Zn-free and thermo-cycled (Table 3c) (Figs. 4·IV, 5·IV). Nevertheless, it augmented ~1.26 fold at intertubular dentin and decreased ~1.09 fold at peritubular dentin when the carious dentin was treated in the same conditions (Table 4c) (Fig. 7·IV); hence, the 1340 cm^{-1} tracing line exhibited a very low level of noise of fluctuation (Fig. 6·IV). On the other hand, α-helices, after Zn-containing restorations applied on caries-affected dentin surfaces attained higher values than the control group, but lower when sound dentin was assessed (Tables 3c, 4c). Interestingly, this orientation-sensitive signal decreased when mineralization was allowed to proceed (Wang et al., 2009).

3.2. Nano-DMA and imaging analysis

To measure the dynamic viscoelastic properties of the dentin substrate, a small sinusoidal force was superimposed on the contact force and the resulting displacement amplitude, and the phase shift between the force and amplitude were measured (Balooch et al., 2004). This force modulation technique was used to quantitatively map the local variation of nanomechanical properties of intertubular and peritubular dentin, using equations (6 and 8). The elastic moduli are obtained by subtracting the stiffness and damping moduli of the sensor, which are the combined values of the sensor and the sample (Hayot et al., 2012). There is a uniform contact area for the tip to probe the surface of the dentin. The displacement amplitude are 0.4 -0.8 nm for the sample scanning parameters. These higher displacement amplitude values are properly extracted from more compliant regions. This is less likely to be negatively impacted at low dynamic measurements on mineral phases. This approach do not risk the fidelity of the measurements conducted in low modulus regions (Wilkinson et al, 2014).

In stiff (mainly elastic) samples such as dentin, the substrate absorbs stress after thermo-cycling (Toledano et al., 2014c), but there will be negligible dissipation of energy by heat and, thus, the damping modulus of the sample results very close to zero (Chuang et al., 2015; Lakes et al., 2001). Consequently, at certain positions within our samples, the actual value of the loss modulus cannot be obtained with confidence. The damping modulus of the sample is masked by the damping modulus of the sensor; thereby, these values are not presented in the manuscript.

The lower mineral-to-matrix ratio assessed in both types of dentin (sound and caries-affected) after Zn-free restorations (Tables 3a, 4a) resulted in a reduced elastic or storage modulus (E') in both substrata, except at intertubular dentin of sound dentin, which performed similar (5.29 *vs* 5.08 GPa, respectively) (Table 2). When thermal

cycling was not applied, the complex modulus (E^*) of sound dentin at peritubular and intertubular dentin were 10.30 and 5.24 GPa, respectively, and the storage moduli, 10.37 and 5.29 GPa, in the same group, expressing stored energy or prestrain energy (Yap et al., 2008). Thus, higher dentin resistance to deformation, *i.e.*, higher E^*, could be seen in Fig. 1·Ia as discontinuous red trace circular-shape formations which represent the greatest complex modulus attained at peritubular dentin, in this experimental group. Similarly, the 3-D contour map of the complex modulus distribution (Fig. 3·Ia) exhibited some rich-areas of higher E^* in the range of ~5-10 GPa of the scale, in the center and right-hand of the image. On the contrary, bigger values of storage modulus were observed as non-regular yellow and red collars of approximately 17-20 GPa (Fig. 2·Ia) in the collected modulus map. Balooch et al., (2004) obtained E^* values of 21 and 48 GPa at intertubular and peritubular, respectively. More recently, Ryou et al., (2015) have accomplished an overall average complex modulus (E^*) of old intertubular and peritubular dentin of ~21 and 31 GPa, and storage moduli (E') values of ~20 and 30 GPa, respectively. Results from scanning mode nano-DMA show that both E^* and E' at peritubular dentin in specimens non thermo-cycled, do not significantly influence the elastic properties of the dynamic mechanical responses for either sound or caries-affected dentin (Table 2). Caries-affected dentin, in the control group, performed similar to sound dentin, at both intertubular dentin and peritubular dentin. Both E^* and E' showed higher values at peritubular dentin than at intertubular dentin (Table 2). This higher resistance to deformation (E^*) corresponded with, *i)* higher intensities of yellow (10-11GPa) and yellow to red (11-12 GPa) colors, forming closed loops at the map of the complex modulus (Fig. 1·Ib), and *ii)* acute peaks of higher intensities (~5-9 GPa) of the scale in 3-D contour map of the complex modulus distribution (Fig. 3·Ib), mostly localized at the bottom of the image. On the contrary, the storage modulus

corresponding to peritubular dentin appeared formed by two eccentric rings of a sharp yellow to red (inner) and wide blue (outer) trace of colors at the corresponding map (Fig. 2·Ib). The discrepancy between results that were obtained could be a result of, but are not limited to, age, race, location or gender of the samples, testing sites, degree of mineralization of peritubular dentin and intertubular dentin, but most importantly to the degree of wetness conditions (Lee et al., 2002a; Angker and Swain, 2006).

The greater relative presence of minerals that attained after thermo-cycling in caries-affected dentin substrata restored with Zn-free restorations became associated to a decrease of the complex modulus at both intertubular and peritubular dentin (Table 2). $E*$ is a measure of the materials resistance to deformation, and it assesses the total elastic and dampening capacity of a material (Equation 5). It encompasses both in-phase and out-of phase response of the sample, from which one calculates the storage modulus E′ and the loss, viscous or imaginary modulus E'', respectively [E*(ω) = E′(ω) + iE″(ω)] (Lee et al., 2002b), where E′ = Re(E*) is the in-phase component of the overall modulus. Storage and viscous moduli account respectively for the energy stored and dissipated. Therefore, it can be estimated that thermal stress produces a decreased resistance to deformation in dentin surface (intertubular and peritubular dentin). This may be attributable to a lower capacity to store and dissipate energy, which is not available for elastic recoil (Espino et al., 2014), in caries-affected dentin substrate restored with Zn-free restorations. The elastic performance of both kind of dentin may be interpreted as images that quantitatively show values variation as different color values. This lower dynamic elastic moduli (Table 2) graphically corresponds with higher intensities of complex modulus at peritubular dentin (15.57 GPa) than at intertubular dentin (3.51 GPa) (Fig. 3·IIb), reflected as a more intense concentration of red color (Fig. 3·IIb/scale) at peritubular locations. Nevertheless, these prominent

higher intensities framed from yellow to red (~8.5-12 GPa) became approximately twofold in sound dentin when observing the tridimensional contour map (Fig. 3·IIa), where the resistance to deformation was 6.71 and 28.03 GPa at intertubular dentin and peritubular dentin, respectively (Table 2). Note that the areas of transition from low $E*$ (intertubular dentin, at sound and caries affected dentin) to higher $E*$ (peritubular dentin, at sound and caries affected dentin) were sharp, denoting a brusque change in properties (Figs. 3·IIa, 3·IIb). The map of the complex modulus, at sound dentin, exhibited clear circles of relevant values, which ranged from blue to red intensities (Fig. 1·IIa), appearing as spheres septum-split in most of the images. On the contrary, on caries-affected dentin surfaces, most of the spheres corresponding to areas of higher $E*$ resulted incomplete and with less intense transition of colors (Fig. 1·IIb). The storage modulus map revealed a diffused distribution of values with poor spatial resolution through the scans (Fig. 2·IIa). The colored marks only exhibited punctual red signals simulating undefined circles of higher E', surrounded by lower E' results. Those circles appeared thicker and more accurate in specimens of caries-affected dentin (Fig. 2·IIb). Thus, the application of modulus mapping to the dentin substrate shows the potential of this technique to reveal property variations with substantially higher spatial resolution. Hence, the complex modulus ($E*$) of caries-affected dentin restored with Zn-containing restorations decreases ~2.55 fold at peritubular dentin, but increased ~1.99 fold at intertubular dentin (Table 2). This elastic response was reflected at the homogeneous redder intensity occupying the biggest part of the intertubular dentin (Fig. 3·IIIb). Thereby, it can be inferred that thermo-cycled Zn-containing restorations favor the intertubular remineralized dentin surface to deformation and damping capacity. The lower E' that was obtained at peritubular dentin in this group, Zn-containing restoration placed on caries-affected dentin substrata, indicates the clear augmentation of the stress

concentration within the peritubular cuff. This observation points out a further failure initiation point at this location (Misra et al., 2004) (Fig. 2·IIIb). On the other hand, if the energy stored becomes too great, as at intertubular dentin (8.07 GPa) (Table 2), then excess of energy would potentially be dissipated through cracking the dentin substrate (Espino et al., 2014). If energy storage and dissipation is altered with thermo-cycling, then the transfer of energy could also be altered. The altered energy transfer to the underlying dentin may have implications for dentin remineralization and remodeling. It is noteworthy to mention that the relative presence of minerals augmented after thermo-cycling at the caries-affected dentin substrata, but without incrementing crystallynity (Tables 3a, 4a). It resulted in a more amorphous crystal which might confer the worst mechanical properties (Scholtanus et al., 2013) to the histological substrate, especially at peritubular dentin (Table 2). In sound dentin, the energy stored diminished by up to 5.48 GPa (Table 2) at intertubular dentin, and to 3.73 GPa at peritubular dentin, in comparison to the caries-affected dentin substratum. The scanning mode nano-DMA analysis of the E' map permitted to observe dense circular areas in blue (~2-3 μm thick) spread out on a green surface with punctual red intensities. Those figures might correspond with the energy stored at tubules (blue), intertubular dentin (green) and peritubular dentin (red) (Fig. 2·IIIa).

It has been stated that thermal stress of dentin results in advance remineralization, represented by new mineral embedded within a preserved collagen network (Toledano et al., 2014c). The mechanism of mineral precipitation also promoted images of higher complex modulus that corresponded with crystal filling of the tubules. This observation was evidenced in the majority of dentin canals in sound dentin (Fig. 3·IIIa), that appeared completely filled with minerals (Fig. 3·IVa). Clear areas of higher resistance to deformation (E^*) were also evidenced in some caries-

affected dentin surfaces (Fig. 3·IIIb). Hence, not all tubules were completely filled, and there was an evident shadow of lumens in the property maps, surrounded by relevant collars of peritubular dentin (Fig. 3·IVb). In sound dentin treated with Zn-containing restorations, it was consistently noted a bigger red scale intensity within the central portion of the occluded lumens, with respect to the adjacent peritubular cuff (Fig. 3·IIIa). Those that were filled did not show a clear transition of complex modulus from the original cuff to the newly mineralized region. It was evident from Table 2, and Figures 3·IIIa and 3·IIIb that the complex modulus of intratubular dentin was ~2.86 fold lower in caries-affected dentin than in sound dentin, though the storage modulus was not significantly different. The scanning mode nano-DMA analysis of the map of the complex modulus at sound dentin exhibited greener zones (arrows) within the collar of higher values of E^* (high red intensity) that might correspond with intratubular precipitates of mineral (Table 2). As a composite material, dentin mechanical properties correspond to the relative proportion of mineral, collagen, and water content (Angker and Swain, 2006). The different visco-elastic properties which show both type of dentin (intertubular dentin and peritubular dentin) could be a result of the high concentration of collagen fibrils in the intertubular dentin. It constitutes an outcome of higher stored potential energy available for elastic recoil (Balooch et al., 2004), giving rise special interest at peritubular dentin (Table 2). At tubular structures, energy dissipation can occur via deformation in axial and radial directions throughout a bridging and frictional pullout procedure which is supported on mineral nucleation at micro and nano-scale levels (Agrawal et al., 2013). Those new radial mineral formations showed, at the 3-D contour map of the complex modulus, a range of values of ~8-15 GPa (blue, green and yellow) (Fig. 3·IIIa). Pullout of stick-slip procedures (Fig. 3·IVa) are well-known mechanisms for energy dissipation, previously studied within nanotube structures

(Agrawal et al., 2013; Grimmer and Dharan, 2009). Irregular circles in blue color extended in a generalized green area with round images of red spots characterized the scan surface of caries-affected dentin after Zn-containing restoration removal (Fig. 1·IIIb).

On the other hand, the elastic, real or storage modulus (E') (Lee et al., 2002b) decreased at intertubular dentin (~3.26 fold) but augmented at peritubular dentin (~1.55 fold) in caries-affected dentin substrate when compared with sound dentin, after restoring with thermo-cycled Zn-free restorations (Table 2). When Zn-containing restorations were used in caries-affected dentin substrata, intertubular dentin attained the highest elastic energy stored or storage modulus (~1.47 fold bigger than in sound dentin). As stated above, storage modulus represents the elastic energy stored which is released after deformation [Ryou et al., 2015; Espino et al., 2014). Dissipation of energy within the structures is of prime importance in dynamic systems (Agrawal et al., 2013) such as the oral function, where teeth and restorations require damping to absorb thermal shock-waves and alleviate stresses. Hence, improving damping characteristics becomes imperative for enhancing their robustness thereby expanding their lifetimes. Transfer of energy during contact from the restorative material to the dentin interface, and from the dentin interface to the underlying dentin may have implications for the elastic response of the dentin-restorative complex interaction. As low modulus regions (peritubular dentin in sound dentin and intertubular dentin in caries-affected dentin) lead to stress concentration in relatively high elastic modulus regions (intertubular dentin in sound dentin and peritubular dentin in caries-affected dentin) (Table 2), the energy stored would potentially be dissipated through cracking the tissue (Misra et al., 2004), *i.e.*, dentin interface. The resistance to deformation and the energy stored between peritubular and intertubular dentin was greater in caries-affected dentin than in sound

dentin treated with Zn-containing amalgams. This produced stress concentration, structure breakdown, and crack-bridging with frictional pullout due to precipitation of minerals. This boots of mineralization, as sight of energy dissipation, contributed to sealing the dentin microcraking, and as result, the clinical performance of this dentin.

Mineral crystallinity (FWHM) expresses the crystallographic or relative atomic order, since narrower peaks suggest less structural variation in bond distances and angles (Schwartz et al., 2012). In general, the narrower the spectral peak width is, the higher the degree of mineral crystallinity (Karan et al., 2009). FWHM increased after observing *data* plotted by the reduced full width and extended height at half maximum of the phosphate band at 961 cm^{-1}, at peritubular dentin of caries-affected dentin surfaces restored with both Zn-free and -containing restorations thermo-cycled (Table 4a) (Fig. 6·IV), in comparison with the untreated group (~1.17 fold lower) (Table 4a). Therefore, this improved crystalline phase or highly ordered chemical structure, which typically shows the lowest energy state of the substrate, correlated with mechanical relaxation associated with atomic motion, *i.e.*, reorganization of the metastable amorphous structure (Lee et al., 2002a). This reorganization toward structures more crystalline matched with peritubular dentin with reduced storage modulus (E') (~2.95 fold at peritubular dentin in sound dentin, and ~3.12 or 1.99 fold at intertubular dentin or peritubular dentin, respectively, in caries-affected dentin) after restoring with Zn-free amalgams, *i.e.*, dentin with lower elastic energy stored (Table 2).

These are, to the best of our knowledge, the only available results from nano-DMA and Raman spectroscopy experiments on dentin interfaces submitted to amalgam restorations and *in vitro* thermal challenge. Thereby, this investigation represents the first attempt to assess the time-dependent behavior and the dentin ability to dissipate mechanical energy, in junction with chemical analysis, of caries-affected dentin exposed

to both Zn-containing restorations and thermo-cycling. These outcomes are important, because they provide information on chemical structure and elastic changes produced at micro and nano-scale, at dentin surfaces. However, additional correlation analyzes with other complementary microscopy techniques as FESEM, EDX, µXRD of sound and caries-affected dentin are still needed. Hence, improving the dissipation of energy within the restorative-dentin interface becomes imperative for enhancing therapy and expanding the lifetime of dental restorations. Further work is now required to determine the mechanism by which thermo-cycling prevent thermal-induced changes in dentin mineralization and dentin strength. Nevertheless, our study also has several weakness; (1), the quantity difference in the major components between both Zn-free and Zn-containing formulations might play a role to the materials performance. This should be considered into future works. (2), Longer duration of thermal loading, inclusion of other remineralizing agents and bioactive ions into the chemical formula of restorative materials, and the effect of the mechanical loading. In addition, to consider other mechanical properties as compressive modulus or fracture modulus in junction with surface topography studies would have expanded the message of this paper, and should have been considered. Future works will also include determining the diffusion of matrix damage and the assessment of visible microcraks. These represent topics for further research. Moreover, these measurements open up the possibility of future probing of other materials-tooth interfaces, *e.g.*, resin-based adhesives and glass-ionomer cements, as well as extending the assessments to other hard tissues as enamel, cementum and bone.

4. Conclusions

1. The low complex and storage modulus of peritubular caries-affected dentin restored with Zn-containing amalgams, in comparison with the intertubular dentin, generates stress concentration, with implications in the mechanical performance of the restored teeth.

2. Caries-affected dentin restored with Zn-containing amalgams achieved higher mineralization and crystallinity, attaining major discrepancy of elastic properties between intertubular and peritubular dentin, than the caries-affected dentin treated with Zn-free restoration. It implies that the transfer of energy is altered at dentin underlying Zn-containing restorations.

3. The different elastic properties attained between intertubular and peritubular dentin, produces higher stored potential energy, and deformation within the dentin substrate in axial and radial directions. It generates bridging and frictional mineral nucleation within the tubules and at intertubular dentin. It occurred due to the increase of the relative presence of minerals and gradient in mineral content.

References

Ager, J.W. 3rd, Nalla, R.K., Balooch, G., Kim, G., Pugach, M., Habelitz, S., Marshall, G.W., Kinney, J.H., Ritchie, R.O., 2006. On the increasing fragility of human teeth with age: a deep-UV resonance Raman study. J. Bone Miner. Res. 21, 1879-1887. DOI: 10.1359/jbmr.060816

Agrawal, R., Nieto, A., Chen, H., Mora, M., Agarwal, A., 2013. Nanoscale damping characteristics of boron nitride nanotubes and carbon nanotubes reinforced polymer composites. ACS Appl. Mater. Interfaces 27, 12052-12057. DOI: 10.1021/am4038678

Almahdy, A., Downey, F.C., Sauro, S., Cook, R.J., Sherriff, M., Richards, D., Watson, T.F., Banerjee, A., Festy, F., 2012. Microbiochemical analysis of carious dentine using Raman and fluorescence spectroscopy. Caries Res. 46, 432-440. DOI: 10.1159/000339487

Angker, L., Swain, M.V., 2006. Nanoindentation: Application to dental hard tissue investigations. J. Mater. Res. 21, 1893-1905. DOI: 10.1557/JMR.2006.0257

Anusavice, K., 2003. Phillips' Science of Dental Materials, 11th ed. Saunders Publishing Co., Elsevier, St. Louis, pp. 832.

Balooch, G., Marshall, G.W., Marshall, S.J., Warren, O.L., Asif, S.A., Balooch, M., 2004. Evaluation of a new modulus mapping technique to investigate microstructural features of human teeth. J. Biomech. 37, 1223-1232. DOI: 10.1016/j.jsb.2008.02.010

Bass, E.C., Wistrom, E.V., Diederich, C.J., Nau, W.H., Pellegrino, R., Ruberti, J., Lotz, J.C., 2004. Heat-induced changes in porcine annulus fibrosus biomechanics. J. Biomech. 37, 233-240. DOI:10.1016/j.jbiomech.2003.07.002

Chuang, S.F., Lin, S.Y., Wei, P.J., Han, C.F., Lin, J.F., Chang, H.C., 2015. Characterization of the elastic and viscoelastic properties of dentin by a nanoindentation creep test. J. Biomech. 16, 2155-2161. DOI: 10.1016/j.jbiomech.2015.01.034

Collins, M.J., Nielsen-Marsh, C.M., Hiller, J., Smith, C.I., Roberts, J.P., Prigodich, R.V., Wess, T.J., Csapò, J., Millard, A.R., Turner-Walker, G., 2002. The survival of organic matter in bone: a review. Archaeometry 44, 383-394. DOI: 10.1111/1475-4754.t01-1-00071

Coutinho, E., Yoshida, Y., Inoue, S., Fukuda, R., Snauwaert, J., Nakayama, Y., De Munck, J., Lambrechts, P., Suzuki, K., Van Meerbeek, B., 2007. Gel phase formation at resin-modified glass-ionomer/tooth interfaces. J. Dent. Res. 86, 656-661. DOI: 10.1177/154405910708600714

Daood, U., Iqbal, K., Nitisusanta, L.I., Fawzy, A.S., 2013. Effect of chitosan/riboflavin modification on resin/dentin interface: spectroscopic and microscopic investigations. J. Biomed. Mater. Res. A 101, 1846-1856. DOI: 10.1002/jbm.a.34482

Donmez, N., Belli, S., Pashley, D.H., Tay, F.R, 2005. Ultrastructural correlates of in vivo/in vitro bond degradation in self-etch adhesives. J. Dent. Res. 84, 355-359. Erratum in: J. Dent. Res., 2006 85. 384. DOI: 10.1177/154405910508400412

Espino, D.M., Shepherd, D.E., Hukins, D.W., 2014. Viscoelastic properties of bovine knee joint articular cartilage: dependency on thickness and loading frequency. BMC Musculoskel. Dis. 15, 205. DOI: 10.1186/1471-2474-15-205

Frank, R.M., Wolff, F., Gutmann, B., 1964. Electron Microscopy of Caries at the Level of Human Dentine. Arch. Oral Biol. 9, 163-179.

Fusayama, T. 1979. Two layers of carious dentin; diagnosis and treatment. Oper. Dent. 4, 63-70.

Fusayama, T., 1993. A simple pain-free adhesive restorative system by minimal reduction and total etching, Ishiyaku EuroAmerica Inc., Tokyo.

Goldin, A., Beckman, J.A., Schmidt, A.M., Creager, M.A., 2006. Advanced glycation end products: sparking the development of diabetic vascular injury. Circulation 114, 597-605. DOI: 10.1161/CIRCULATIONAHA.106.621854

Grimmer, C.S., Dharan, C.K.H., 2009. High-cycle fatigue life extension of glass fiber/polymer composites with carbon nanotubes. J. Wuhan Univ. 24, 167-173. DOI: 10.1007/s11595-009-2167-4

Han, L., Grodzinsky, A.J., Ortiz, C., 2011. Nanomechanics of the Cartilage Extracellular Matrix. Annu. Rev. Mater. Res. 41, 133–168. DOI:10.1146/annurev-matsci-062910-100431

Hayot, C.M., Forouzesh, E., Goel, A., Avramova, Z., Turner, J.A., 2012. Viscoelastic properties of cell walls of single living plant cells determined by dynamic nanoindentation. J. Exp. Bot. 63, 2525-2540. DOI: 10.1093/jxb/err428

Hertz, H., 1881. Über die Berührung fester elastischer Körpen (On the contact of rigid elastic solids). J. Reine Angew. Math. 92, 156-171.

Hoppe, A., Güldal, N.S., Boccaccini, A.R., 2011. A review of the biological response to ionic dissolution products from bioactive glasses and glass-ceramics. Biomaterials 32, 2757-2774. DOI: 10.1016/j.biomaterials.2011.01.004

Jastrzebska, M., Wrzalik, R., Kocot, A., Zalewska-Rejdak, J., Cwalina, B., 2003. Raman spectroscopic study of glutaraldehyde-stabilized collagen and pericardium tissue. J. Biomater. Sci. Polym. Ed. 14, 185-197. DOI: 0.1163/156856203321142605

Karan, K., Yao, X., Xu, C., Wang, Y., 2009. Chemical profile of the dentin substrate in non-carious cervical lesions. Dent. Mater. 25, 1205-1212. DOI: 10.1016/j.dental.2009.04.006

Krafft, C., Steiner, G., Beleites, C., Salzer, R., 2009. Disease recognition by infrared and Raman spectroscopy. J. Biophotonics 2, 13-28. DOI:10.1002/jbio.200810024

Lakes, S.R., Lee, T., Bersie, A.,Wang, Y.C., 2001. Extreme damping in composite materials with negative-stiffness inclusions. Nature 410, 565-567. DOI: 10.1038/35069035

Lee, M.L., Li, Y., Feng, Y.P., Carter, C.W., 2002a. Study of frequency dependence modulus of bulk alloy around the glass transition by dynamic mechanical analysis. Intermetallics 10, 1061-1064. DOI: 10.1016/S0966-9795(02)00143-7

Lee, S.W., Hinsberg, W.D., Kanazawa, K.K., 2002b. Determination of the viscoelastic properties of polymer films using a compensated phase-locked oscillator circuit. Anal. Chem. 74, 125-131. DOI: 10.1021/ac0108358

Liu, Y., Tjäderhane, L., Breschi, L., Mazzoni, A., Li, N., Mao, J., Pashley, D.H., Tay, F.R., 2011. Limitations in bonding to dentin and experimental strategies to prevent bond degradation. J. Dent. Res. 90, 953-968. DOI: 10.1177/0022034510391799

Marshall Jr., G.W., Marshall, S.J., Kinney, J.H., Balooch, M., 1997. The dentin substrate: structure and properties related to bonding. J. Dent. 25, 441-458. DOI: 10.1016/S0300-5712(96)00065-6

Marshall, G.W., Habelitz, S., Gallagher, R., Balooch, M., Balooch, G., Marshall, S.J., 2001. Nanomechanical properties of hydrated carious human dentin. J. Dent. Res. 80, 1768-1771. DOI: 10.1177/00220345010800081701

Mazzitelli, C., Monticelli, F., Toledano, M., Ferrari, M., Osorio, R., 2012. Effect of thermal cycling on the bond strength of self-adhesive cements to fiber posts. Clin. Oral Investig. 16, 909-915. DOI 10.1007/s00784-011-0576-1

Miles, C.A., Ghelashvili, M., 1999. Polymer-in-a-box mechanism for the thermal stabilization of collagen molecules in fibers. Biophys. J. 76, 3243-3252. DOI: 10.1016/S0006-3495(99)77476-X

Milly, H., Festy, F., Watson, T.F., Thompson, I., Banerjee, A., 2014. Enamel white spot lesions can remineralise using bio-active glass and polyacrylic acid-modified bio-active glass powders. J. Dent. 42, 158-166. DOI: 10.1016/j.jdent.2013.11.012

Misra, A., Spencer, P., Marangos, O., Wang, Y., Katz, J.L., 2004. Micromechanical analysis of dentin/adhesive interface by the finite element method. J. Biomed. Mater. Res. B 70, 56-65. DOI: 10.1002/jbm.b.30012

Oliver, W.C., Pharr, G.M., 1992. An improved technique for determining hardness and elastic modulus using load and displacement sensing indentation experiments. J. Mater. Res. 7, 1564-1583. DOI: 10.1557/JMR.1992.1564

Opdam, N.J., Bronkhorst, E.M., Loomans, B.A., Huysmans, M.C., 2010. 12-year survival of composite vs. amalgam restorations, J. Dent. Res. 89, 1063-1067. DOI: 10.1177/0022034510376071

Osorio, R., Yamauti, M., Osorio, E., Ruiz-Requena, M.E., Pashley, D.H., Tay, F.R., Toledano, M., 2011. Zinc reduces collagen degradation in demineralized human dentin explants. J. Dent. 39, 148-153. DOI: 10.1016/j.jdent.2010.11.005

Penel, G., Delfosse, C., Descamps, M., Leroy, G., 2005. Composition of bone and apatitic biomaterials as revealed by intravital Raman microspectroscopy. Bone 36, 893-901. DOI:10.1016/j.bone.2005.02.012

Ryou, H., Romberg, E., Pashley, D.H., Tay, F.R., Arola, D., 2015. Importance of age on the dynamic mechanical behavior of intertubular and peritubular dentin. J. Mech. Behav. Biomed. Mater. 42, 229-242. DOI:10.1016/j.jmbbm.2014.11.021

Saito, M., Fujii, K., Marumo, K., 2006. Degree of mineralization-related collagen crosslinking in the femoral neck cancellous bone in cases of hip fracture and controls. Calcif. Tissue Int. 79, 160-168. DOI: 10.1007/s00223-006-0035-1

Saito, M., Marumo, K., 2013. Bone quality in diabetes. Front. Endocrinol. (Lausanne) 14, 72. DOI: 10.3389/fendo.2013.00072

Salehi, H., Terrer, E., Panayotov, I., Levallois, B., Jacquot, B., Tassery, H., Cuisinier, F., 2013. Functional mapping of human sound and carious enamel and dentin with Raman spectroscopy. J. Biophotonics 6, 765-774. DOI: 10.1002/jbio.201200095

Scholtanus, J.D., van der Hoorn, W., Ozcan, M., Huysmans, M.C., Roeters, J.F., Kleverlaan, C.J., Feilzer, A.J., 2013. Staining of dentin from amalgam corrosion is induced by demineralization. Am. J. Dent. 26, 185-190. DOI: 10.5167/uzh-89940

Schwartz, A.G., Pasteris, J.D., Genin, G.M., Daulton, T.L., Thomopoulos, S., 2012. Mineral distributions at the developing tendon enthesis. PLoS One 7, e48630. DOI: 10.1371/journal.pone.0048630

Sell, D.R., Monnier, V.M., 1989. Structure elucidation of a senescence cross-link from human extracellular matrix. Implication of pentoses in the aging process. J. Biol. Chem. 264, 21597-21602

Spencer, P., Ye, Q., Misra, A., Goncalves, S.E., Laurence, J.S., 2014. Proteins, pathogens, and failure at the composite-tooth interface. J. Dent. Res. 93, 1243-1249. DOI: 10.1177/0022034514550039

Strehle, M.A., Rösch, P., Petry, R., Hauck, A., Thull, R., Kiefer, W., Popp, J., 2004. A Raman spectroscopic study of the adsorption of fibronectin and fibrinogen on titanium dioxide nanoparticles. Phys. Chem. Chem. Phys. 6, 5232-5236. DOI: 10.1039/B406524G

Takatsuka, T., Tanaka, K., Iijima, Y., 2005. Inhibition of dentine demineralization by zinc oxide: in vitro and in situ studies. Dent. Mater. 21, 1170-1177. DOI: 10.1016/j.dental.2005.02.006

Timlin, J.A., Carden, A., Morris, M.D., Rajachar, R.M., Kohn, D.H., 2000. Raman spectroscopic imaging markers for fatigue-related microdamage in bovine bone. Anal. Chem. 72, 2229-2236. DOI: 10.1021/ac9913560

Toledano, M., Aguilera, F.S., Cabello, I., Osorio, R., 2014a. Remineralization of mechanical loaded resin-dentin interface: a transitional and synchronized multistep process. Biomech. Model. Mechanobiol. 13, 1289-1302. DOI: 10.1007/s10237-014-0573-9

Toledano, M., Aguilera, F.S., Osorio, E., Cabello, I., Osorio, R., 2014c. Microanalysis of thermal-induced changes at the resin-dentin interface. Microsc. Microanal. 20, 1218-1233. DOI: 10.1017/S1431927614000944

Toledano, M., Aguilera, F.S., Osorio, E., Cabello, I., Toledano-Osorio, M., Osorio, R., 2015a. Mechanical and chemical characterisation of demineralised human dentine after amalgam restorations. J. Mech. Behav. Biomed. Mater. 47, 65-76. DOI: 10.1016/j.jmbbm.2015.03.012

Toledano, M., Aguilera, F.S., Osorio, E., López-López, M.T., Cabello, I., Toledano-Osorio, M., Osorio, R., 2015b. On modeling and nano-analysis of caries-affected dentin restored with Zn-containing amalgam and in vitro oral function. Biointerphases 10: 041004. DOI: 10.1116/1.4933243

Toledano, M., Aguilera, F.S., Sauro, S., Cabello, I., Osorio, E., Osorio, R., 2014b. Load cycling enhances bioactivity at the resin-dentin interface. Dent. Mater. 30, e169-e188. DOI: 10.1016/j.dental.2014.02.009

Vanna, R., Ronchi, P., Lenferink, A.T., Tresoldi, C., Morasso, C., Mehn, D., Bedoni, M., Picciolini, S., Terstappen, L.W., Ciceri, F., Otto, C., Gramatica, F., 2015. Label-free imaging and identification of typical cells of acute myeloid leukaemia and myelodysplastic syndrome by Raman microspectroscopy. Analyst 140, 1054-1064. DOI: 10.1039/c4an02127d

Vaseenon, S., 2011. Relationship between caries-affected dentin mineral density and microtensile bond strength, Master's thesis, University of Iowa.

Wang, C., Wang, Y., Huffman, N.T., Cui, C., Yao, X., Midura, S. Midura, R.J., Gorski, J.P., 2009. Confocal laser Raman microspectroscopy of biomineralization foci in UMR 106 osteoblastic cultures reveals temporally synchronized protein changes preceding and accompanying mineral crystal deposition. J. Biol. Chem. 284, 7100-7113. DOI: 10.1074/jbc.M805898200

Wang, S.Y., Cappellini, E., Zhang, H.Y., 2012. Why collagens best survived in fossils? Clues from amino acid thermal stability. Biochem. Biophys. Res. Commun. 422, 5-7. DOI: 10.1016/j.bbrc.2012.04.122

Wang, Y., Spencer, P., Walker, M.P., 2007. Chemical profile of adhesive/caries-affected dentin interfaces using Raman microspectroscopy. J. Biomed. Mater. Res. A 81, 279-286. DOI: 10.1002/jbm.a.30981

Wang, Y., Yao, X., 2010. Morphological/chemical imaging of demineralized dentin layer in its natural, wet state. Dent. Mater. 26, 433-442. DOI: 10.1016/j.dental.2010.01.002

Watkins, J.H., Nakajima, H., Hanaoka, K., Zhao, L., Iwamoto, T., Okabe, T., 1995. Effect of zinc on strength and fatigue resistance of amalgam. Dent. Mater. 11, 24-33. DOI: 10.1016/0109-5641(95)80005-0

Weiner, S., Traub, W., Wagner, H.D., 1999. Lamellar bone: structure-function relations. J. Struct. Biol. 30, 241-255. DOI:10.1006/jsbi.1999.4107

Wilkinson, T.M., Zargari, S., Prasad, M., Packard, C.E., 2015. Optimizing nano-dynamic mechanical analysis for high-resolution, elastic modulus mapping in organic-rich shales. J. Mater. Sci. 50, 1041-1049. DOI: 10.1007/s10853-014-8682-5

Xu, C., Wang, Y., 2011. Cross-linked demineralized dentin maintains its mechanical stability when challenged by bacterial collagenase. J. Biomed. Mater. Res. B Appl. Biomater. 96, 242-248. DOI: 10.1002/jbm.b.31759

Xu, C., Wang, Y., 2012. Collagen cross linking increases its biodegradation resistance in wet dentin bonding. J. Adhes. Dent. 14, 11-18. DOI:10.3290/j.jad.a21494

Yap, H.W., Lakes, R.S., Carpick, R.W., 2008. Negative stiffness and enhanced damping of individual multiwalled carbon nanotubes. Phys. Rev. B 77, 045423. DOI: 10.1103/PhysRevB.77.045423

Zhang, L., Morsi, Y, Wang, Y., Yubao, L., Ramakrishna, S., 2013. Review scaffold design and stem cells for tooth regeneration. Jpn. Dent. Sci. Rev. 49, 14-26. DOI:10.1016/j.jdsr.2012.09.001